Unexpected softening of a fibrous matrix by contracting inclusions

Mainak Sarkar,[a] Brian M. Burkel,[b,c] Suzanne M. Ponik,[b,c] Jacob Notbohm[a,c,*]

[a] Department of Mechanical Engineering, University of Wisconsin–Madison, Madison, WI, USA
[b] Department of Cell and Regenerative Biology, University of Wisconsin–Madison, Madison, WI, USA
[c] University of Wisconsin Carbone Cancer Center, Madison, WI, USA
[*] Corresponding author: Jacob Notbohm, jknotbohm@wisc.edu, Ph: (608) 890-0030

Abstract

Cells respond to the stiffness of their surrounding environment, but quantifying the stiffness of a fibrous matrix at the scale of a cell is complicated, due to the effects of nonlinearity and complex force transmission pathways resulting from randomness in fiber density and connections. While it is known that forces produced by individual contractile cells can stiffen the matrix, it remains unclear how simultaneous contraction of multiple cells in a fibrous matrix alters the stiffness at the scale of a cell. Here, we used computational modeling and experiments to quantify the stiffness of a random fibrous matrix embedded with multiple contracting inclusions, which mimicked the contractile forces of a cell. The results showed that when the matrix was free to contract as a result of the forces produced by the inclusions, the matrix softened rather than stiffened, which was surprising given that the contracting inclusions applied tensile forces to the matrix. Using the computational model, we identified that the underlying cause of the softening was that the majority of the fibers were under a local state of axial compression, causing buckling. We verified that this buckling-induced matrix softening was sufficient for cells to sense and respond by altering their morphology and force generation. Our findings reveal that the localized forces induced by cells do not always stiffen the matrix; rather, softening can occur in instances wherein the matrix can contract in response to the cell-generated forces. This study opens up new possibilities to investigate whether cell-induced softening contributes to maintenance of homeostatic conditions or progression of disease.

Keywords

Extracellular Matrix, Fiber Network, Stiffness, Cell–Matrix Interaction, Buckling

1. Introduction

Many tissues are composed of cells encapsulated in a three-dimensional fibrous extracellular matrix [1]. Cells remodel the matrix, either biochemically by synthesis and degradation of the matrix, or mechanically by virtue of their contractility [2–5]. The cell-matrix interaction is bidirectional [6], meaning that cellular contractility is tuned by the stiffness of the matrix surrounding the cell [7–10], while cell forces can also modify matrix stiffness, for example, by mechanically stiffening the matrix at the scale of the bulk material [11, 12]. Cells sample the matrix not at the bulk scale, but rather at scales of tens of microns, which renders knowledge of the bulk matrix stiffness insufficient to predict cell sensing at the microscale. Several studies deciphered that individual contracting cells can mechanically stiffen the matrix at these small length scales [13–15], but tissues rarely contain solitary cells; rather, it is common for multiple contracting cells to be interspersed within the same matrix. Due to the effects of nonlinearity and complex force transmission pathways within the matrix, it remains unclear how collective contraction by multiple cells affects the mechanics and whether those collective effects are sufficiently large for cells to sense and respond.

We focus here on the question of how multiple contracting cells within a random fibrous matrix alter the stiffness. Despite the common understanding that an individual contractile cell stiffens the matrix, a few recent reports studying multi-cellular matrices, wherein cells were either seeded on decellularized matrices [16] or embedded inside collagen matrices [17, 18], described a contradicting observation, that contracting cells soften the matrix at the scale of tens of microns. This softening is often thought to be a consequence of matrix degradation due to cell-secreted metalloproteinases [17, 18]. The role of mechanical cell-matrix interactions, if any, in instrumenting such softening is not yet clear. In this light, prior studies on multi-cellular interactions in fibrous matrices observed the existence of complex mechanical coupling between contracting cells [19, 20], which results in cell-mediated global contraction of the matrix [2, 21], however, the current literature lacks a clear quantification of the changes in fiber structure and mechanical stiffness resulting from the contraction of multiple cells.

Here, we combined experiments and simulations to study how multiple contracting cells mechanically alter the stiffness of the matrix. Focusing solely on the mechanical interactions between the cells and the matrix is challenging given the potential of cells to biochemically remodel the matrix. To mitigate this challenge, we studied an analogous system wherein cells were replaced with contracting inclusions made of poly(N-isopropylacrylamide) (PNIPAAm), which could not degrade or synthesize the matrix as cells do. In parallel, we used mechanics-based computational models of inclusion-matrix systems, wherein the inclusions contracted, and we studied the resulting matrix fiber deformations and mapped them to the matrix stiffness. We validated the model results by performing microscopic indentation experiments on PNIPAAm-embedded collagen matrices. Finally, we verified that the changes in matrix stiffness caused by local contraction of PNIPAAm microspheres could be sensed by cells by measuring cellular morphology and cell-induced matrix displacements.

2. Methods

2.1. Preparation of Collagen Matrix with Embedded Contracting Microspheres

Thermosensitive microspheres of poly(N-isopropylacrylamide) (PNIPAAm) with average diameter ≈ 65 μm were prepared as described in our prior work [22]. These microspheres were treated to covalently bind to the collagen fibers using sulfo-SANPAH as previously described [22]. Treated microspheres were mixed with neutralized rat tail collagen I (Corning, Inc.) to make matrices with random fibrous structure having a final collagen concentration of 3 mg/mL, as previously described [22]. As these collagen matrices were heated from 22°C to 39°C, the embedded PNIPAAm microspheres contracted by $\approx 40\%$ [23], thereby applying microscale displacements in the matrices mimicking the displacements induced by contracting

cells.

2.2. Rheometry of the Bulk Matrix

A commercial rheometer (Kinexus Ultra+, Malvern Pananlytical) was used to quantify the global shear modulus of the PNIPAAm-embedded collagen matrices. To grip the collagen matrices to the rheometer, two functionalized glass coverslips (treated with 0.5% (3-aminopropyl)triethoxysilane and 0.5% gluteraldehyde) were adhered to the flat plate geometries of the rheometer by double sided acrylic adhesives (3M Inc.). Cylindrical collagen matrices with a radius of 9 mm, and a height of 1.77 mm were polymerized between these two coverslips on the rheometer at 22°C for 90 min. A schematic of the test setup is depicted in Fig. 1a. Small shear strains were induced by twisting the matrix about its axis. The maximum shear strain applied was 0.36% to remain in the linear regime of deformation. To ensure that the loading was quasi-static, we kept the maximum strain rate below 0.02% /s. The angular acceleration was below 1.17×10^{-5} rad/s^2, meaning that inertial loads were negligible. To measure the shear modulus (G_0), we fitted a line to the data of torque versus angle and applied the standard equation for torsion. For each matrix, the shear modulus was first measured at 22°C, and then the temperature of the matrix was increased to 39°C (chosen to be substantially above the phase transition temperature of PNIPAAm, to induce maximal contraction). We waited for 1 hr for the temperature of the matrix to equilibrate, and the shear modulus at 39°C was measured.

2.3. Experiments Quantifying the Mechanics of Collagen Matrices at Scales of a Cell

2.3.1. Matrix Preparation

Treated PNIPAAm microspheres were mixed with neutralized collagen labeled with Alexa Fluor 488, as described in our prior work [22]. The collagen concentration was 3 mg/mL, and collagen matrices were polymerized into disks of 20 mm diameter and 1.6 mm thickness in glass-bottom dishes at 26°C for 45 min, resulting in a random network of fibers (Supplemental Fig. S10). To ensure that the collagen fibers did not adhere to the glass, the surfaces of the glass bottom dishes were pre-treated with a solution of 4% pluronic acid (Sigma-Aldrich) for at least 24 hr. The PNIPAAm microspheres were observed to sink to the bottom of the collagen matrices during polymerization. Upon heating to 37°C, the collagen matrices contracted globally. The concentration of PNIPAAm microspheres in the collagen matrices produced a global matrix contraction of $\approx 27\%$ at 37°C (Supplemental Fig. S10b). Additional collagen matrices were made without the PNIPAAm microspheres; these matrices were unaffected by temperature changes and served as controls.

2.3.2. Microscopic Indentation

We measured the stiffness of the top surfaces of the collagen matrices using microscopic indentation experiments, as elaborated in the following three steps.

First, glass microspheres with nominal diameter 138 μm and density 2.5 g/cm^3 (Cospheric) were used as spherical indenters. These micro-indenters were mixed with 1× phosphate buffered saline (PBS) and sparsely spread on the top surfaces of the collagen matrices just before imaging. Since the actual diameters of these indenters were not constant and varied between 120 μm and 160 μm, the diameter of each indenter was measured by manual image analysis.

Second, the matrices were fully submerged in 1× PBS, and image stacks of their top surfaces were collected on a Nikon upright FN1 confocal microscope. These stacks contained images of Alexa-488 labelled collagen fibers which were excited by the 488 nm laser, with emission collected by high sensitivity GaAsP detectors and recorded in Nikon NIS-Elements software. A 25× water immersion objective with numerical aperture 1.1 (Nikon) was used, and the lens of the objective remained submerged inside the PBS and above the surface of the matrix as depicted schematically in Supplemental Fig. S11a. Image stacks were collected

with a step size of 1 μm. Images were scanned at 1024×1024 pixels with a pixel size of 0.499×0.499 μm^2.

Third, we analyzed the images to determine the actual diameter of each indenter and the corresponding indentation depth. Briefly, the z cross-section of the image stack through an indenter was imported into a vector graphics editor (Adobe Illustrator) and a circle was manually fitted to match the profile of the indented regime. The diameter of this circle was the actual diameter of the spherical indenter, and the indentation depth (δ) was determined by measuring the depth of penetration in a direction perpendicular from the surface of the matrix. Knowing the diameter of the indenter and considering its buoyancy in PBS, we calculated the component of the effective weight of the indenter along the direction of the indentation depth. The ratio of the effective weight of the indenter and the indentation depth was computed to determine the secant stiffness of the matrix at the location of each indenter.

2.3.3. Experiments with Cells

MDA-MB-231 cells and MDA-MB-231 cells expressing Lifeact-GFP were cultured in high glucose Dulbecco's Modified Eagle's Medium (DMEM) with 10% fetal bovine serum at 37°C and 5% CO_2. Medium from cell culture was collected, centrifuged, and the supernatant was used as conditioned medium in later experiments.

Both control and PNIPAAm-embedded collagen matrices were floated in 1× PBS at 37°C for 45 min, during which time the PNIPAAm-embedded matrices radially contracted. After warming the matrices, the PBS was removed and the matrices were washed with DMEM, which was pre-warmed at 37°C. Then the medium was removed and $\approx 20,000$ MDA-MB-231 cells were seeded near the center of the matrices. The cells were allowed to adhere to the collagen matrix for 45 min at 37°C before adding DMEM supplemented with conditioned medium at a 1:5 ratio. The cells were allowed to spread for 18 hr. For assessing morphological features, we used matrices with unlabelled collagen fibers; these matrices were fixed with paraformaldehyde, and the cells were stained with Alexa-488 phalloidin (Invitrogen, R37110). For assessing the cell-induced displacements, we used Alexa-594 labelled collagen and cells expressing Lifeact-GFP.

The cells and the matrix fibers were imaged on a Bruker Ultima Multiphoton microscope equipped with a Coherent Charmeleon Ti-Sapphire laser and Hamamatsu multi-alkali photomultipliers. The matrices were excited at 890 nm and a 20× air objective with numerical aperture 0.45 (Nikon) was used for imaging. A $445/40$ nm filter was used to capture the second harmonic generation (SHG), while a $525/70$ nm and 565 nm long-pass filters were used to capture the green and red fluorescence, respectively. For assessing cellular morphology, stacks of images were collected with a step size of 5 μm and the images were scanned at 1024×1024 pixels with a pixel size of 0.347×0.347 μm^2. For studying cell-mediated matrix deformation, time lapse image-stacks were collected over a period of 48 min and the stacks had a step size of 2.5 μm; these images were scanned at 1024×1024 pixels with a pixel size of 0.293×0.293 μm^2. During the time lapse acquisitions, the matrices with live cells were placed in a commercial stage top incubator (Okolab), which was maintained at 37°C and 5% CO_2.

For evaluating cell morphology, images were analyzed in ImageJ to identify the boundaries of each cell. For each cell, we quantified shape by measuring the length of its longest axis (feret's diameter) and the ratio of the square of the cell perimeter to the cell area. For evaluating cell-induced matrix displacements, displacement fields were computed with Fast Iterative Digital Image Correlation [24] using a subset size of 64×64 pixels (18.75×18.75 μm^2) and a subset spacing of 16 pixels (4.69 μm), to correlate pairs of images separated by 48 min, similar to our prior work [22, 25–28]. Considering each cell to act like a dipole, we identified the center and the alignment of this analogous dipole by inspecting the displacement fields in the matrix. To identify the regions in the matrix most affected by cellular forces, we used the continuum mechanics solution for the displacement field due to a force dipole, which defined a dumbell-shaped region of large cell-induced displacements. Finally, for each cell, the 80th percentile of the magnitude of the matrix

displacement inside the dumbell-shaped region was computed as a measure of displacement induced by that cell.

2.4. Computational Modeling

2.4.1. Finite Element Model of Inclusion-Matrix Systems

To model fibrous matrices with fully embedded inclusions, we constructed two-dimensional (2D) networks of randomly oriented fibers; see Supplemental Note 1 for justification of the use of 2D models. The fiber networks were designed to match the architecture of type I collagen using a modified version of a previously developed algorithm [29–31]. Firstly, this algorithm randomly deposits a set of nodes in a 2D domain and connects them with fibers. Then it uses a simulated annealing-based optimization technique to move the nodes and swap the fibers connecting at different nodes until a desired average fiber length (L_f) and connectivity (defined as the number of fibers connecting each node) is achieved. Noting that collagen matrices have nodal connectivity less than Maxwell's isostatic threshold (which is twice the system dimension) [29, 32], we developed sub-isostatic 2D matrices with a connectivity of 3.4, which matches that of collagen [29, 30] and is below the 2D isostatic threshold of 4. Our matrix models had regions where fibers crossed but did not connect, similar to observations from images of collagen matrices [26, 33]. The matrix generation algorithm is available in a public repository at `https://github.com/jknotbohm/fiber_network_model`.

The fibers in the matrix were modeled as linear elastic Timoshenko beams whose shearing stiffness was half of the axial stiffness. The fibers were soft in bending and had the ratio of bending stiffness to axial stiffness, $\kappa = 1 \times 10^{-4}$, which is a value typically reported for type I collagen fibers [34–37]. In the finite element software, we used two three-node quadratic beam elements for each fiber, and the fibers were "welded" at the connections to transmit both forces and moments. Circular inclusions were introduced inside the domain of the matrix, and their diameters matched the relative sizes of PNIPAAm microspheres in experimental matrices (diameters $\geq 2L_f$). To add the inclusions to the fiber network, fibers with end nodes inside the region of an inclusion were trimmed at their intersection with the periphery of the inclusion. Fibers crossing the inclusions were kept. The circular inclusions were filled with three-node continuum triangle elements which underwent isotropic thermal contraction. Additional cross-links connected the matrix fibers to the inclusions to obtain a fully connected system. These cross-links were two-node linear beams which transferred forces and moments between the matrix and the inclusions. These cross-links and inclusions had the same Young's modulus as that of the matrix fibers. The size of the matrix models was always $\geq 30L_\mathrm{f}$, and the models contained two or more embedded inclusions.

2.4.2. Boundary Conditions and Finite Element Simulations

All simulations were performed with multiple load steps, wherein one load step was used to induce contraction of the inclusions and separate load steps were used to measure the matrix stiffness. When inducing contraction of the inclusions, both free and fixed external boundaries were used, as described in the Results section. To characterize how the contracting inclusions influenced the global shear modulus of the matrices, two load steps were used, the first being contraction of the inclusions, and the second being a simple shear boundary condition. To measure the stiffness of the matrix at length scales that would be sensed by cells, stiffness was measured by contracting dipoles of different orientations introduced in the matrix at various locations as described in the Results. The dipoles were two-node truss elements of length $2L_\mathrm{f}$, and their end points were connected to nodes in the matrix. Each dipole underwent thermal contraction such that the dipole was under a state of local equilibrium. The Young's modulus of the dipoles was six orders of magnitude larger than that of the matrix fibers to ensure that the thermal strain of the dipoles was the same as the actual strain. The internal force in the dipole at 10% axial contraction was extracted. The ratio of this internal force and the dipole displacement gave the secant stiffness of the matrix microenvironment sensed by the dipole. All finite element simulations were performed on Abaqus (Dassault Systèmes). Given

that large local deformations were produced inside the matrix, we used the implicit dynamic quasistatic solver with the option of nonlinear geometry, as in our prior work [27, 38, 39]. During post-processing, we characterized the local matrix mechanics at the level of the fibers by identifying force chains and quantifying fiber excess lengths (difference between the fiber's contour length and the node-to-node distance), similar to our prior work [39].

2.5. Statistical analysis

Statistical analysis was performed in MATLAB R2020a. Statistical tests used were the sign test, Wilcoxon rank sum test, and Kruskal-Wallis test for, respectively, one, two, more than two groups of data, as indicated in the figure captions. To define the level of significance of the correlation between two different parameters, a Pearson's test was used. Values of $p < 0.05$ were considered statistically significant. For binary events, we used a bootstrapping approach (with $10,000$ iterations) to obtain the 95% confidence interval.

3. Results

3.1. PNIPAAm–Matrix System Behaves Analogously to the Cell–Matrix System

To begin our study on the effects of multiple contracting cells on the mechanics of fibrous matrices, we considered the global shear modulus, which has been commonly studied. For example, the presence of uniaxial global pretension increases the global shear modulus of the fibrous extracellular matrix [35, 37, 40, 41]. Similarly, contracting cells or contracting inclusions induce local pretensions inside the matrix resulting in an increase in the global shear modulus of the matrix [11, 12, 42]. Here, we began by verifying these findings using contracting PNIPAAm microspheres, which produce well-controlled forces and do not degrade or synthesize matrix as cells do. We cast collagen matrices embedded with PNIPAAm microspheres and, using a shear rheometer, measured their shear moduli (G_0) at the global scale at low strains before and after contraction of the embedded microspheres (Fig. 1a), expecting to observe stiffening caused by contraction, similar to a recent study [42]. For nine independent PNIPAAm–matrix systems, the average value of G_0 was 65.7 Pa when the microspheres were in the uncontracted state (at 22°C, Fig. 1b). When the system temperature was raised from 22°C to 39°C to induce contraction of the embedded microspheres, the modulus G_0 increased to an average value of 206 Pa (Fig. 1b), which was 3.1 times the global shear modulus at 22°C. To verify that the contracting microspheres alone altered modulus, and that the change of temperature had no mechanical effect on the collagen matrix, we conducted control experiments on collagen matrices in the absence of PNIPAAm microspheres. Results from eight independent control collagen matrices showed no clear effect of the temperature change on the global shear modulus of the control matrices (Fig. 1c), similar to our prior studies [22, 28]. The factor of 3.1 stiffening caused by contraction of the PNIPAAm microspheres is similar to the typical extent of the macroscale stiffening exhibited by cell–matrix systems due to cellular contractions [11, 12].

Given that the contracting inclusions only interact mechanically with the surrounding collagen matrix, the experimentally observed macroscale stiffening of the system is a mechanical phenomenon, which we further validated by simulating these boundary conditions with mechanics-based models of the fibrous matrices (Fig. 1d). These models contained a cluster of inclusions embedded in a fiber matrix and, the inclusions were radially contracted by 40%. Next, we imitated the boundary condition of the shear rheometer (Fig. 1d,e) and computed the small-strain global shear modulus of the models before and after the contraction of inclusions, G_1 and G_2, respectively. For six independent inclusion-matrix models, contracted inclusions increased the global shear modulus by an average factor of $G_2/G_1 = 3.1$ (Fig. 1f), similar to the bulk stiffening exhibited by PNIPAAm-matrix systems.

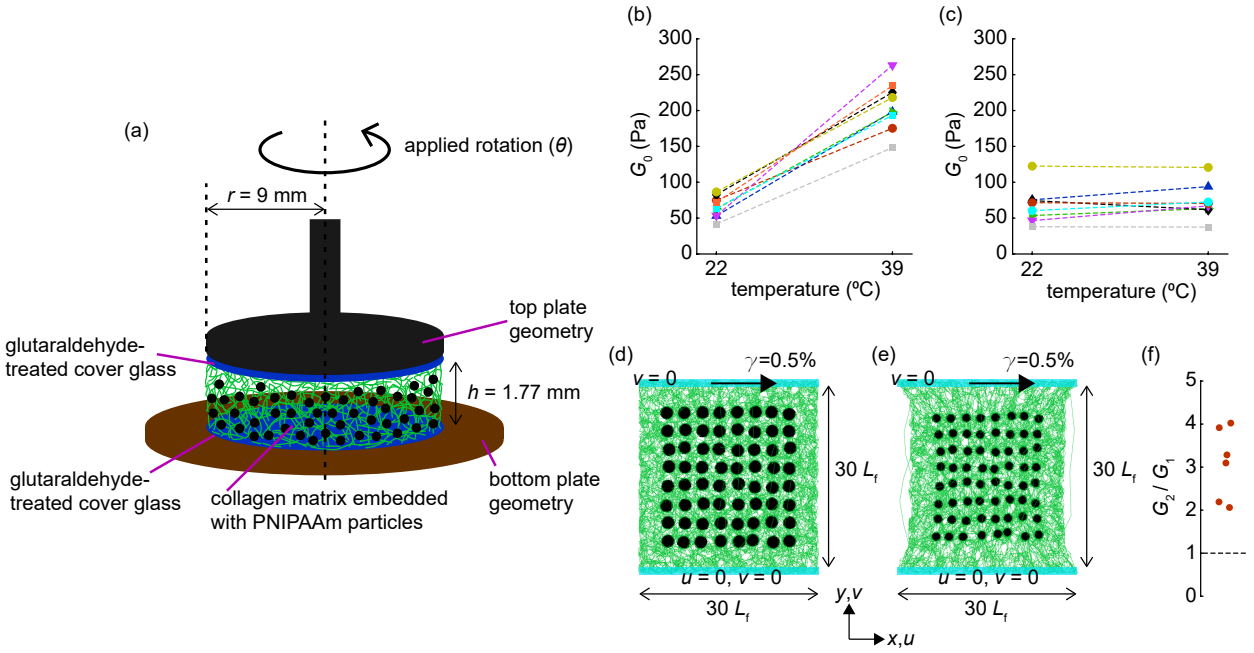

Figure 1: Experiments and simulations characterizing the global modulus of fibrous matrix with contracting inclusions. (a) Diagram of experiments with the rheometer. A collagen matrix with embedded PNIPAAm microspheres was polymerized between the two coverslips attached to the parallel plates of the rheometer, and the top plate was axially rotated to twist the sample. (b) Small strain shear modulus (G_0) of nine independent PNIPAAm-embedded matrices measured before and after the contraction of embedded PNIPAAm microspheres, respectively at temperatures 22°C and 39°C. The increase in the shear modulus from 22°C to 39°C is statistically significant ($p = 0.0039$, sign test). (c) Small strain shear modulus (G_0) of eight independent control collagen matrices at temperatures 22°C and 39°C. The temperature change had no significant effect on the modulus ($p = 1$, sign test). (d) Simulation on an equivalent 2D matrix model with multiple inclusions and simple shear boundary conditions. Prior to the contraction of these inclusions, the shear modulus at 0.5% shear strain was quantified and defined as G_1. (e) The deformed model after the contraction of inclusions by 40%, with the shear modulus at 0.5% shear strain called G_2. (f) Ratios G_2/G_1 for six independent models were always greater than unity, indicating global stiffening of the matrix due to contracted inclusions.

3.2. Simulations on Fiber Matrix with Contracting Inclusions

We observed in the previous section that the contracting microspheres stiffened the matrix under conditions of simple shear. These contracting microspheres mimicked cell contraction in cell-matrix systems studied in prior work, wherein cell contraction induced similar stiffening of the matrix under the same conditions of simple shear [11, 12]. Similarly, single contracting cells can increase the matrix stiffness at scales of tens of microns [13–15]. However, for the case of multiple cells contracting in a random fibrous matrix, it is not clear that the changes in matrix stiffness could be sensed by a cell, because at this scale, the matrix exhibits spatial heterogeneity in which the stiffness can vary by more than an order of magnitude [23, 28, 43–46]. Thus, the influence of multiple contracting cells on the matrix stiffness at the length scale of a cell remains an open question.

To determine how multiple contracting cells could alter the matrix stiffness at scales sensed by a cell, we began with computational modeling of the contracting inclusions and fibrous matrix. The models consisted of multiple inclusions, each of diameter $D = 2L_f$, randomly embedded inside the fibrous matrix at an average inter-inclusion spacing $\approx 1.5L_f$ (Fig. 2a). Without constraining the outer boundaries of the matrix, the embedded inclusions were radially contracted by 40%, causing them to locally pull on the surrounding matrix fibers, mimicking forces produced by cells. In response to these tensile forces, fibers oriented perpendicular to the periphery of each inclusion were axially stretched, constituting force chains (Fig. 2b). These tensile force chains are expected to be associated with stiffening of the matrix [39, 47, 48].

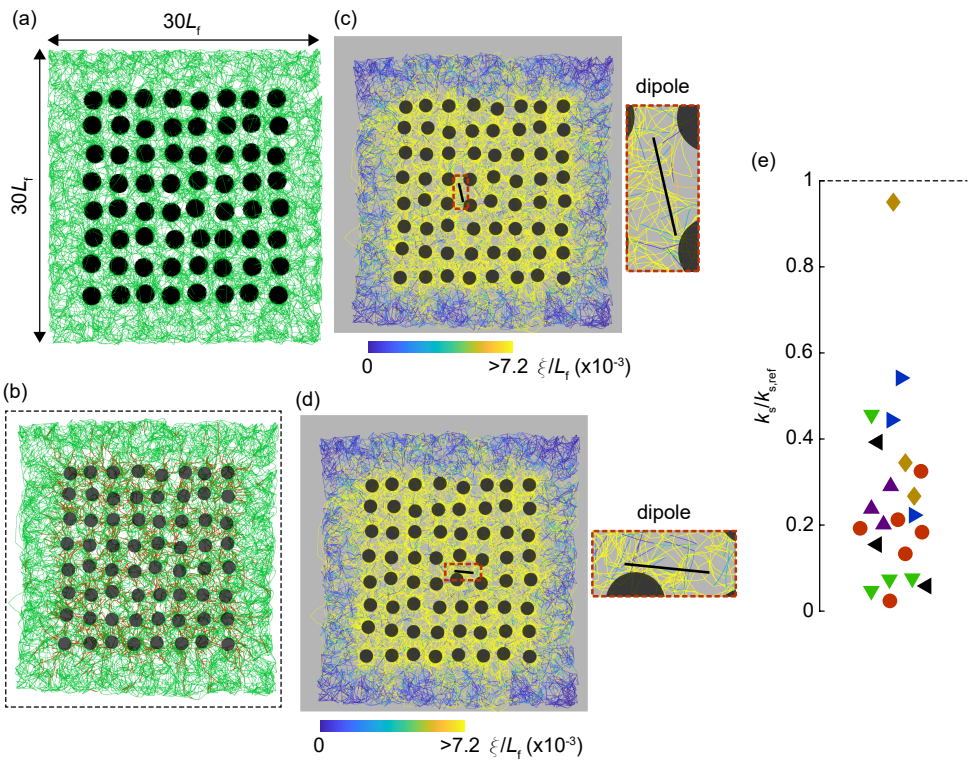

Figure 2: Effect of a group of contracting inclusions on stiffness at the scale of a cell. (a) A representative undeformed state of the matrix containing a cluster of inclusions. The inclusions had a diameter of $D = 2L_f$ and were randomly embedded inside the matrix at an average inter-inclusion spacing of $\approx 1.5L_f$. (b) After inclusions contracted by 40%, the network globally contracted (uncontracted matrix size shown by the dashed box). Force transmission is shown by force chains constituting the top 20% highly stretched fibers in the matrix (red). These force chains emanated radially from the periphery of the inclusions. (c, d) The deformed matrix (of panel b) with a contracting dipole in the inter-inclusion space as depicted by the black line. Panels c and d depict two different representative orientations of the dipole. Insets depict the enlarged views of the respective dipole. The fibers of the deformed matrix are color coded based on the normalized values of their excess lengths (ξ/L_f). The dipoles contracted and registered the stiffness of the matrix inside the inter-inclusion space. (e) For differently aligned dipoles and for six independent matrices, the ratio of the values of matrix stiffness sensed by the dipole after and before the contraction of inclusions ($k_s/k_{s,ref}$) were recorded. $k_s/k_{s,ref} < 1$ indicates matrix softening due to contracting inclusions. Each marker indicates a different dipole; each marker shape indicates a different independent fiber network.

To determine how the contracting inclusions altered the matrix stiffness, we measured the stiffness at different locations and in different directions, using contracting dipoles, each of which mimicked the contraction of a cell, as shown in Figs. 2c,d. The dipoles contracted and sensed the stiffness, similar to the way a cell senses its microenvironment. Each dipole axially contracted by 10%, and the ratio of internal force and the contracted displacement was computed to quantify the secant stiffness. Surprisingly, the values of stiffness measured after the contraction of the inclusions, k_s, were always less than those measured before the contraction of the inclusions, $k_{s,ref}$, meaning that the contracting inclusions mechanically changed the microenvironment of the dipole. This mechanical change, as indicated by the values of $k_s/k_{s,ref} < 1$ indicated matrix softening (Fig. 2e). Dipoles aligned in various different directions across six independent fiber network models all showed softening, indicating the softening was consistent and occurred in all directions (Fig. 2e). To investigate why the contracting inclusions caused the matrix to soften, we investigated the deformed microstructure of the matrix at the level of fibers. Despite the fact that the contracting inclusions induced tensile force chains (Fig. 2b), the majority of the matrix fibers ($\approx 60\%$) were not stretched, but rather in a state of axial compression, potentially causing buckling. To quantify buckling of the fibers, we

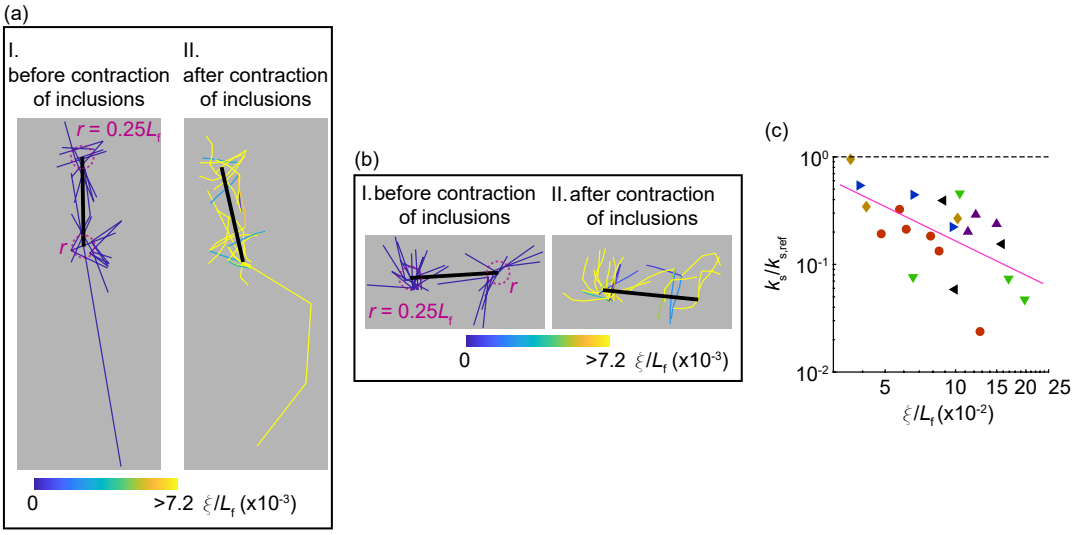

Figure 3: Simulations on inclusion-matrix models relate fiber buckling to matrix softening. (a, b) Enlarged views of the dipoles of Fig. 2c and d, respectively, along with nearby matrix fibers before (I) and after (II) the contraction of the inclusions. Fibers are color coded by normalized excess length ξ/L_f. After contraction of the inclusions, the fibers are highly buckled, as indicated by the large excess lengths. The fibers constituting the microenvironment of the dipole were defined using circles of radius $r = 0.25L_f$ at the end points of the dipole. (c) Scatter plot of normalized stiffness ($k_s/k_{s,ref}$) sensed by each dipole against average excess length (ξ/L_f) in the vicinity of that dipole. The values of $k_s/k_{s,ref}$ were always less than one, indicating that the matrix softened at the scale of the dipoles. The correlation between the reduction in matrix stiffness and excess lengths was statistically significant ($p = 0.0076$, Pearson). Each marker type indicates a dipole from an independent model.

computed and mapped each fiber's excess length, defined as the difference between the contour length of the fiber and its node-to-node distance [49] (Fig. 2c,d). Fibers circumferential to the periphery of the inclusions had large excess lengths, indicating buckling.

To establish if the fiber excess lengths were the cause of the softening, we focused in detail on the excess lengths of the fibers near to each contracting dipole. Considering that the fibers closest to each dipole's end points have the largest effect on the mechanics sensed by that dipole, we defined circular regions of radius $0.25L_f$ surrounding the end points of each dipole; all fibers passing through these circular regions defined the microenvironment of that dipole (e.g., Fig. 3a, I and Fig. 3b, I). In the microenvironment of the dipole, the initially undeformed fibers (Fig. 3a, I and Fig. 3b, I) buckled after the contraction of the inclusions, and accumulated excess lengths (Fig. 3a, II and Fig. 3b, II). These observations remained consistent across multiple independent inclusion-matrix models, and an additional representative example is depicted in Supplemental Fig. S1. Measurements from several independent dipoles in six different models revealed a statistically significant correlation between the extent of matrix softening and the average excess length of the fibers in the microenvironment of the dipoles ($p = 0.0076$, Pearson) (Fig. 3c). Therefore, the multiple contracting inclusions buckled the majority of the matrix fibers, thereby triggering softening in the matrix in all directions.

To consider other loading conditions, we repeated the simulations after replacing the contracting circular inclusions with contracting dipoles, which might more closely resemble contracting cells. As above, the dipoles contracted in the first load step with free boundaries, and another dipole was used to measure the stiffness before and after contraction. In these simulations, the trends were the same, namely that the matrix softened in all directions and the degree of softening was correlated to the amount of fiber buckling present (Supplemental Fig. S2). Next, we designed a simulation to measure stiffness at a different length scale,

namely at the scale of the global material. To this end, we embedded inclusions in the fibrous matrix, and, after inducing contraction of the inclusions under free boundary conditions, we applied simple shear, observing global softening caused by the contracting inclusions (Supplemental Fig. S3). Lastly, to verify that fiber buckling is essential for the softening, we repeated the simulations with the contracting circular inclusions in matrices having fixed boundaries. Compared to free boundaries, the fixed boundaries had greatly reduced excess lengths, indicating the fixed boundaries suppressed fiber buckling (Supplemental Fig. S4a–h). In turn, the matrix softening was largely eliminated, with some dipoles sensing a stiffer local environment caused by the contracting inclusions and some sensing approximately the same stiffness as before contraction of the inclusions (Supplemental Fig. S4i). Together, these findings indicate that when the boundary conditions allow the matrix to contract, the localized forces produced by contracting inclusions induce fiber buckling that leads to matrix softening.

3.3. Simulations on Fiber Matrix with Two Contracting Inclusions

We noted in the prior section that multiple contracting inclusions softened the matrix. To better understand the mechanics and the role of underlying system length scales that tuned this unexpected softening, we studied simplified inclusion-matrix models with only two embedded inclusions. To this end, two inclusions, each of diameter $D = 2L_f$ and separated by a variable inter-inclusion spacing d, were embedded inside matrices with free boundaries (Fig. 4a). Prior models showed substantial fiber alignment and densification between the pairs of contracting inclusions in fibrous materials [40, 50–53], but such alignment and densification was not present here, which is due to the fact that the inclusions were simulated by elastic elements that are able to move closer together upon contraction, which is required to maintain force equilibrium (see Supplemental Fig. S5 and Supplemental Note 2 for more details).

A dipole of length $2L_f$ was introduced in the matrix between the two inclusions (Fig. 4a), and the dipole was initially oriented perpendicular to the common center line of the inclusions. As in the previous section, we identified the microenvironment of the dipole by defining threshold circles of radius $0.25L_f$ at the end points of the dipole, and the excess lengths of all the fibers passing through these circular regions were quantified (Fig. 4b). The contracting dipoles were again used to measure the matrix stiffness. Similar to the results with the multi-inclusion systems, the values of stiffness after the contraction of the inclusions, k_s, were smaller than those measured prior to the contraction of the inclusions, $k_{s,ref}$ for all inter-inclusion spacing d, in four independent models, again indicating softening (Fig. 4c). To investigate how the contracting inclusions softened the matrix, we again characterized force chains and excess lengths. Each contracting inclusion pulled the radially aligned fibers, and similar to Fig. 2b, we mapped the force chains, which were perpendicular to the periphery of the inclusions (Fig. 4d,g,j). Again similar to Fig. 2c,d, matrix fibers aligned parallel to the periphery of the contracting inclusions had large excess lengths (Fig. 4e,h,k). We verified that the excess lengths appropriately indicated fiber buckling by noting the positive correlation between excess length and normalized curvature of the fibers (Supplemental Fig. S6). We also tested the effect of magnitude of contraction on matrix softening, observing that both excess lengths and the extent of softening were correlated to the amount of radial contraction (Supplemental Fig. S7).

Next, we studied how the ratio of the two system length scales, the inter-inclusion spacing (d) and the inclusion diameter (D), tuned the geometric proximity of the dipole from the contracted inclusions to influence the matrix in the dipole microenvironment. To this end, the excess lengths of the fibers (ξ) in the vicinity of the dipole, as identified in Fig. 4b, were calculated and mapped (Fig. 4f). We conducted a parametric study by varying the inter-inclusion spacing (d) alone (e.g., Figs. 4g,h,j,k), and mapped the fibers in the dipole microenvironment based on their excess lengths (e.g., Figs. 4i,l), similar to Fig. 4f. From a qualitative evaluation of Figs. 4f,i,l, when inter-inclusion spacing d decreased, there was an increase in the number of highly buckled fibers in the dipole microenvironment. At each value of the parameter d/D, we quantified the average excess length of fibers in the microenvironment of the dipole (ξ/L_f). Results

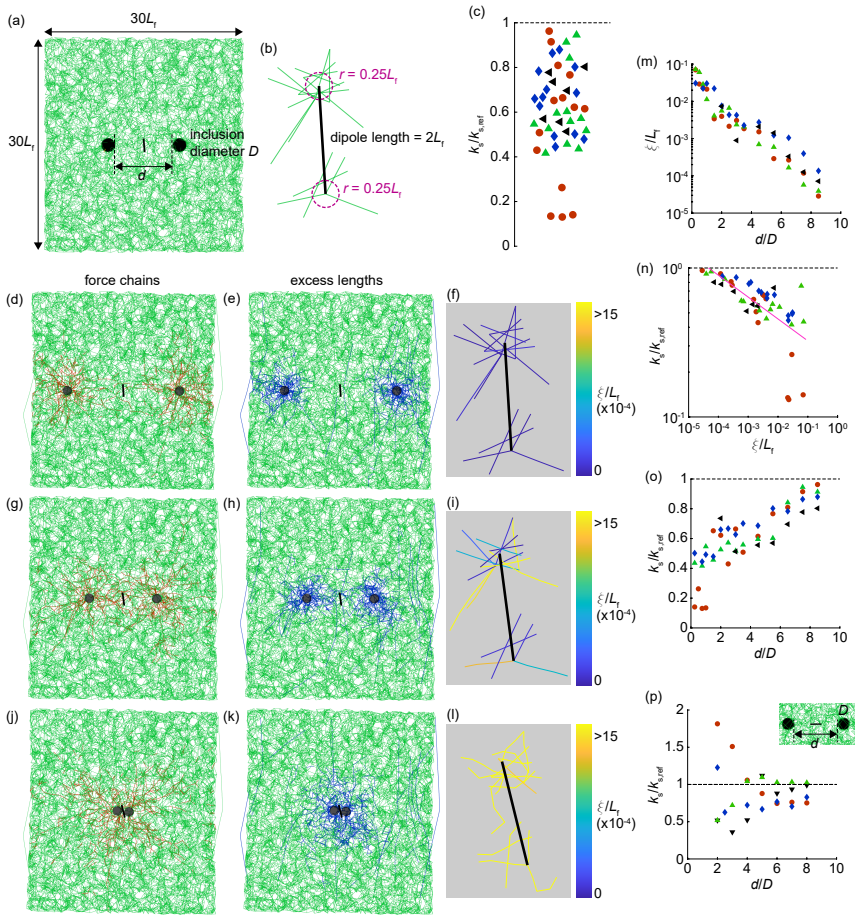

Figure 4: Simulations on matrix models containing two contracting inclusions. (a) A representative model containing two inclusions of diameter $D = 2L_f$, separated by inter-inclusion spacing d. The central dipole of length $2L_f$ is transverse to the imaginary line joining the centers of the inclusions. The inclusions were radially contracted by 40%. (b) Enlarged view of the central dipole which samples fibers passing through the circular regions of radius $0.25L_f$ centered at the dipole's end points. (c) For four independent matrices, the ratio of the values of matrix stiffness sensed by the dipole after and before the contraction of inclusions ($k_s/k_{s,ref}$) were recorded, with $k_s/k_{s,ref} < 1$ indicating softening. Each marker color indicates an independent model. (d) A representative deformed state of the matrix with $d = 8.5D$, where the force chains consisting of top 5% most stretched fibers are shown in red. (e) The deformed matrix of panel d, where the top 5% most buckled fibers are shown blue. (f) The dipole of the system described in panels d and e. The matrix fibers in its microenvironment are colored based on the values of their excess lengths. (g, h, i) A representative deformed state of the matrix with $d = 4.5D$, where the force chains, buckled fibers, and dipole are shown, similar to panels d–f. (j, k, l) A representative deformed state of the matrix with $d = 0.5D$, where the force chains, buckled fibers, and dipole are shown, similar to panels d–f. (m) Plot showing the dependence of the average excess length of fibers in the microenvironment of the dipole to the model parameter d/D. (n) The normalized matrix stiffness in the vicinity of the transverse dipole ($k_s/k_{s,ref} < 1$) was negatively correlated to the average excess length of fibers in the microenvironment of the dipole. (o) The normalized matrix stiffness ($k_s/k_{s,ref}$) against the model parameter d/D. Panels a–o considered the transversely aligned dipole of panel a. (p) The matrix stiffness in the direction longitudinal to the imaginary center-line of the inclusions (inset) was plotted against the model parameter d/D. More than half (18 out of 28 instances, 95% confidence interval [13, 23]) of the data points exhibited $k_s/k_{s,ref} < 1$, indicating softening. In panels m–p, each marker color indicates an independent model. In panels c & n–p, the black dashed line at $k_s/k_{s,ref} = 1$ indicates no matrix softening.

from four independent matrix models consistently revealed a negative correlation between ξ/L_f and d/D (Fig. 4m). A second parametric study considering variable inclusion diameter D (Supplemental Fig. S8a–k) exhibited similar dependence between ξ/L_f and d/D (Supplemental Fig. S8l).

Interestingly, as the average excess length of the fibers in the microenvironment of the dipole increased,

so did the extent of softening in the matrix (Fig. 4n and Supplemental Fig. S8m), meaning that the presence of soft buckled fibers mechanically softened the matrix microenvironment. As noted in Fig. 4m and Supplemental Fig. S8l, the parameter d/D governed the extent of fiber buckling, and these soft buckled fibers modified the stiffness of the matrix in the microenvironment of the dipole (Fig. 4n and Supplemental Fig. S8m). Consequently, the softening of the inclusion-matrix systems could be tuned by changing the value of the system parameter d/D (Fig. 4o and Supplemental Fig. S8n). This observation remains valid as long as the inter-inclusion spacing and the inclusion diameter exceeds the fiber length. Therefore, the microenvironment over which a cell (or an analogous dipole) samples the matrix is independently tuned not by the fiber length, but by the ratio of the inter-inclusion spacing and the inclusion diameter.

The analysis thus far depicted softening in the direction transverse to the center-line of the inclusions, and notably the matrix fibers predominantly buckled in this direction as well (Figs. 4e,h,k and Supplemental Figs. S8d,g,j). Recalling our observations on matrices with many contracting inclusions that dipoles oriented in all directions sensed matrix softening (Fig. 2e), we wanted to investigate how the contracted inclusions altered the mechanics sensed by dipoles in other orientations, in particular in the orientation longitudinal to the center-line of the inclusions, where we would expect the fibers to be predominantly under a state of tension. In this case, one would expect the matrix to stiffen in the region between the inclusions, because tensile force chains exist along this axis (Fig. 4d,g,j). We modeled longitudinal dipoles between the inclusions and repeated the parametric study of Fig. 4o. Contrary to our expectation, results from four independent matrices frequently showed softening (Fig. 4p). Specifically, 18 out of 28 data points (95% confidence interval, $[13, 23]$ out of 28 data points) in Fig. 4p exhibited softening with $k_s/k_{s,\mathrm{ref}} < 1$.

To investigate further, we considered that buckling-induced softening would likely result from negative (contractile) normal strain. Thus, we computed the normal strain along the dipole axis, $\varepsilon_{\parallel}$. We first analyzed the case of dipoles oriented transverse to the axis connecting the inclusions, for which the normal strain was negative, with both excess lengths and softening strongly correlated with $-\varepsilon_{\parallel}$ (Supplemental Fig. S9a,b). We also compared $-\varepsilon_{\parallel}$ against the distance between contracting inclusions, d/D, wherein there was a clear monotonic trend (Supplemental Fig. S9c). Next, we analyzed the surprising case of the dipole aligned along the axis connecting the contracting inclusions, for which the stiffness ratio $k_s/k_{s,\mathrm{ref}}$ was correlated to the strain along the dipole axis $\varepsilon_{\parallel}$ (Supplemental Fig. S9d). Importantly, for all cases of softening ($k_s/k_{s,\mathrm{ref}} < 1$), $\varepsilon_{\parallel}$ was negative. A negative value of $\varepsilon_{\parallel}$ may seem unexpected but is consistent with the observation that the contracting inclusions are able to move closer together (Supplemental Fig. S5). Finally, we computed $\varepsilon_{\parallel}$ for the case of many contracting inclusions (Supplemental Fig. S9e–g), observing that $\varepsilon_{\parallel}$ was always negative, consistent with the fact that softening was always observed for the case of multiple contracting inclusions with free external boundaries (Figs. 2–3).

3.4. Experimental Assessment of the Mechanics of PNIPAAm-Embedded Matrices

Next, we designed an experiment to test the model prediction that contractile inclusions lead to softening of matrices having free boundaries. The need for free boundaries mean that experimental testing using a rheometer, as in Fig. 1, was not possible, because gripping the matrices with the rheometer would prevent the global contraction of the matrix. Therefore, we designed an experiment that would measure matrix stiffness in a matrix that was free to contract. To this end, we used an indentation experiment (similar to Ref. [54]). We cast collagen matrices embedded with PNIPAAm microspheres, used glass microspheres as indenters, and imaged them with a confocal microscope to quantify the indentation depths (δ), which were typically in the tens of microns. Before inducing contraction of the PNIPAAm microspheres (*i.e.*, at 22°C), the microscale indentation depth δ was typically ≈ 45 μm, both in the absence and presence of PNIPAAm microspheres (e.g., Fig. 5a,b and Fig. 5c,d). Similarly, at 37°C, the indentation δ for control matrices without the PNIPAAm microspheres was near 45 μm, suggesting that the matrix stiffness was unaffected by the temperature change (Fig. 5e,f), similar to our earlier macroscale observation (Fig. 1c). When heated to

37°C, thereby inducing contraction of the PNIPAAm microspheres, global matrix shrinking occurred with in-plane stretch ratios of ≈ 0.73 and an associated increase in fiber density (Supplemental Fig. S10). The indentation depth δ was larger than before matrix shrinking, typically ≈ 76 µm (e.g., Fig. 5g–l), indicating the occurrence of a mechanically soft microenvironment below the indenters.

The indentation depths δ resulted from the weight of the indenter alone, as there was negligible adhesion between the indenters and the matrix, as verified from the obtuse contact angles between indenters and matrix (Supplemental Fig. S11b). We further noted that in a region below the indenters, the fibrous matrix was always densified (Supplemental Fig. S11c–e). Such densification was expected from the predictions of a recent numerical study [55], which identified that this densification results from nonlinearity in the fibrous matrix, and highlights that the force–displacement relationship for indentation of a fibrous matrix is strongly different than that for a linear elastic matrix. To quantify the stiffness of the matrices, we computed the ratio of indenter weight and indentation depth. The values of stiffness in control and PNIPAAm-embedded matrices at multiple independent locations were quantified. For matrices at 22°C with and without PNIPAAm microspheres, there was no significant difference in stiffness, indicating no effect of the PNIPAAm microspheres themselves. Additionally, control matrices without microspheres that were heated to 37°C had no significant difference in stiffness, indicating no effect of the temperature change on stiffness. Compared to these controls, matrices with contracted PNIPAAm microspheres exhibited a statistically smaller stiffness (k_s), by factor of > 2 (Fig. 5m). Therefore, even though the multiple contracting microspheres increased the local fiber density, the buckling enabled by contraction of these unrestrained matrices outweighed the local increase in density, in turn leading to mechanical softening, confirming our model predictions.

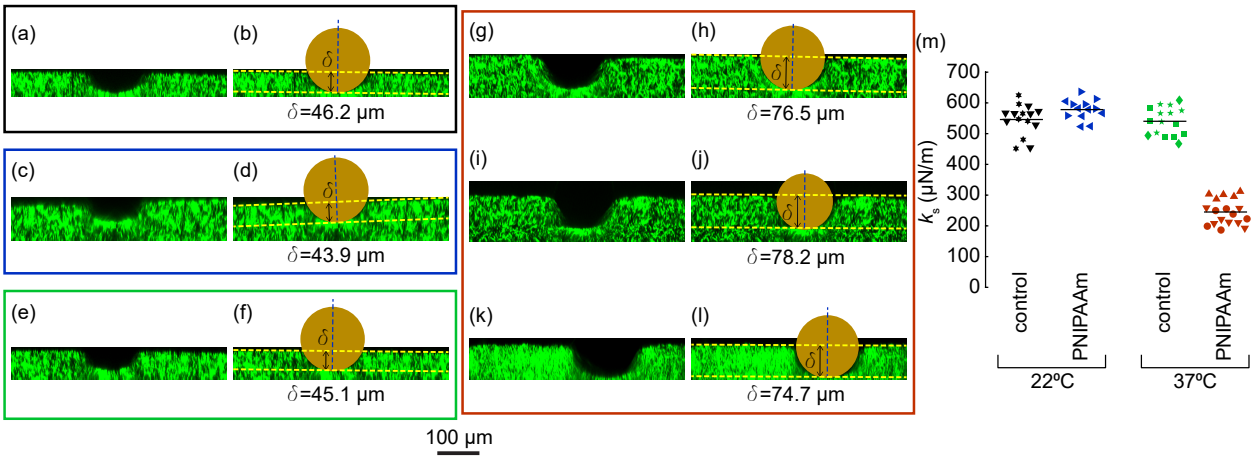

Figure 5: Micro-indentation experiments. (a) A representative cross-section of a control collagen matrix without the PNIPAAm microspheres at room temperature (22°C), when indented by a spherical micro-indenter at its surface. (b) The fitted circle represents the indenter, and its measured diameter (148 µm) was used to compute its weight. The slight inclination of the surface of the matrix (dashed yellow line) with the horizontal (0.66°) was taken into account to calculate the component of the weight perpendicular to the matrix surface. The depth of indentation was the perpendicular indentation depth ($\delta = 46.2$ µm) from the matrix surface. (c,d) A representative cross-section and fitted circle of a collagen matrix with the PNIPAAm microspheres at room temperature (22°C), when these PNIPAAm microspheres did not contract. (e,f) A representative cross-section and fitted circle of a control collagen matrix without the PNIPAAm microspheres at elevated temperature (37°C). (g–l) Representative cross-sections and fitted circles of collagen matrices with the PNIPAAm microspheres at elevated temperature (37°C), when the PNIPAAm microspheres contracted. (m) The values of secant stiffness (k_s) measured by multiple different indenters are plotted. The values of stiffness of the control matrices and PNIPAAm-matrices were plotted at 22°C and 37°C, and they were segregated in four groups. Notably, the matrices with PNIPAAm microspheres at the elevated temperature (37°C) exhibited significant decrease in stiffness in contrast to the other three groups ($p = 9.7 \times 10^{-9}$, Kruskal-Wallis test). Markers with an identical shape and color indicate independent indenters from one sample. The black lines represent mean values of the respective data set.

3.5. Cells Sense and Respond to the Mechanics of PNIPAAm-Embedded Matrices

Finally, we questioned whether the reduction in matrix stiffness caused by local contraction of PNIPAAm microspheres could be sensed by cells. To this end, we prepared additional collagen matrices and seeded MDA-MB-231 breast carcinoma cells onto them with the goal of observing cellular functions on both the contracted PNIPAAm-embedded matrices and on the matrices of pure collagen, which served as controls. Before seeding cells, PNIPAAm-embedded matrices exhibited global radial contraction by $\approx 27\%$, and as the micro-indentation experiments revealed, these contracted matrices were more compliant than control at scales of tens of microns. Matrix stiffness affects the morphology of breast cancer cells [56, 57], with softer matrices generally inducing the cells to become more rounded and less elongated. In this light, we assessed the cellular morphology in control and contracted matrices to determine whether the cells sensed the soft contracted matrices. The cells were more elongated in the stiff control matrices, whereas their morphology was more rounded in the soft contracted matrices (Fig. 6a,b and Supplemental Fig. S12). We quantified the morphology of each cell in the control and contracted matrices by calculating their feret's diameter (the longest cell axis) and the ratio of the square of the cell perimeter P to the cell area A. In contrast to the cells on the control matrices, cells on the softer contracted matrices had significantly smaller feret's diameters (Fig. 6c). Also, the cells on the contracted matrices were more circular with significantly smaller values of P^2/A (Fig. 6d). As it is unlikely that the change in local fiber density due to microsphere contraction caused these effects on cell morphology (see Supplemental Note 3), these data suggest that the contraction-induced matrix softening was sufficient for the cells to sense it.

With this evidence that the cells sensed the softening induced by the contracting PNIPAAm microspheres, we further investigated whether those cells responded by producing different displacement fields within the matrix, as the forces produced by the cells typically increase with an increase in matrix stiffness [7–10]. To this end, we collected time-lapse images of the single cells and the matrix (Fig. 6e and Fig. 6g) and applied image correlation to matrix images separated by 48 min to quantify the cell-induced matrix displacement fields. Considering that the PNIPAAm-embedded matrices were softer than the control matrices, displacements in PNIPAAm-embedded matrices of magnitude equal to or less than those in the stiffer control matrices would indicate smaller cell contractility in PNIPAAm-embedded matrices compared to control. Representative results showed that the cell-induced matrix displacements appeared far smaller in the PNIPAAm-embedded matrices compared to control (Fig. 6e–h). Considering that the cell sampled the fibrous matrix analogously to a contracting dipole, we identified the regions in the matrix most affected by cell forces by using the continuum mechanics solution for the displacement field produced by a dipole to define a dumbell-shaped region within which the displacements were expected to be largest (Fig. 6e–h). The 80th percentile of the magnitude of the matrix displacement within these regions was computed as a measure of the cellular response in the control and PNIPAAm-embedded matrices. Compared to control matrices, the cell-induced matrix displacement was nearly a factor of three smaller in the contracted PNIPAAm-embedded matrices (Fig. 6i). This observation, combined with the fact that the stiffness of PNIPAAm-embedded matrices is smaller than control by a factor > 2 indicates a drastic reduction in cell-generated forces in the PNIPAAm-embedded matrices, which further confirms cell sensing and response to the altered matrix stiffness.

4. Discussion

While the matrix near an individual contractile cell is known to stiffen, the effect of multiple contracting cells on the matrix stiffness at the scale of a cell has not been quantified. Here, using both modeling and experiments of matrices with random fiber organization, we mimicked cell contraction using contracting inclusions and quantified the effects on the stiffness of the matrix, both at the global scale and at the scale of a cell. Upon contraction of the embedded inclusions, matrices with free boundaries consistently softened,

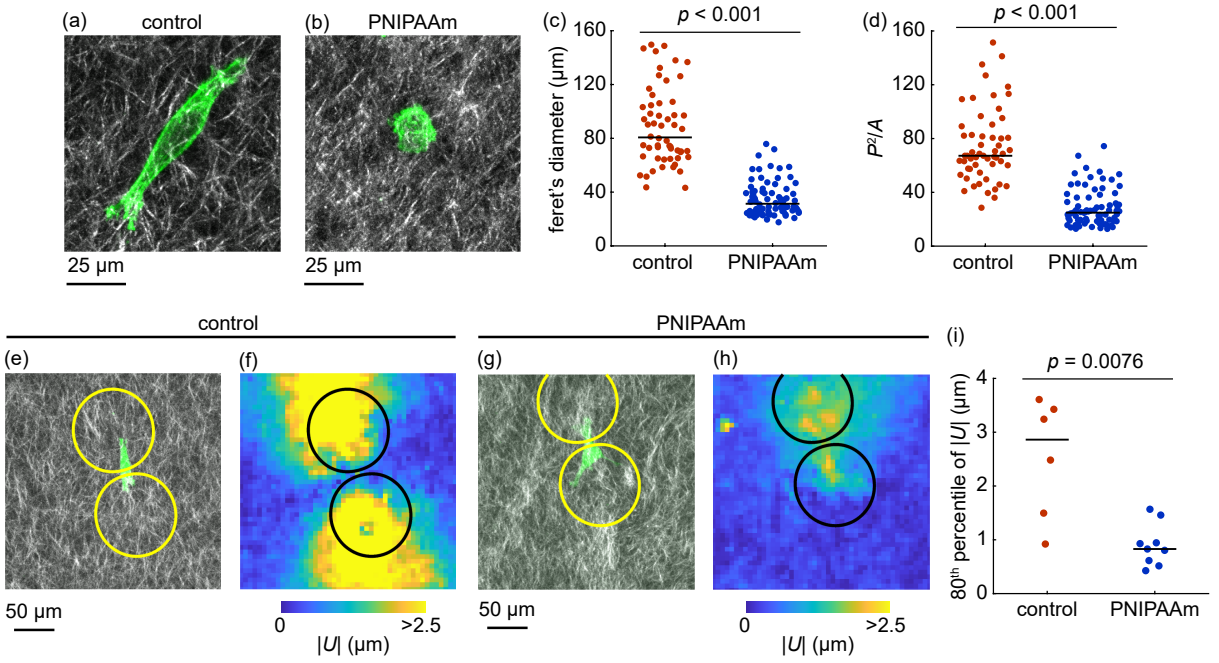

Figure 6: Experiments depicting stiffness sensing and response by MDA-MB-231 cells. (a) Representative elongated morphology of a cell in a control matrix of collagen, with no embedded PNIPAAm microspheres at 37°C. (b) Representative rounded morphology of a cell in a PNIPAAm-embedded collagen matrix, when the embedded PNIPAAm microspheres contracted at 37°C. (c) For many independent cells in control and PNIPAAm-matrices, the length of the longest axis (feret's diameter) was measured. In the contracted PNIPAAm-matrices, the cells had significantly smaller feret's diameter ($p = 8 \times 10^{-21}$, rank sum). (d) For many independent cells in control and PNIPAAm-matrices, the ratio of the square of the cell perimeter (P) to the cell area (A) was computed. In the contracted PNIPAAm-matrices, P^2/A was significantly smaller ($p = 4 \times 10^{-19}$, rank sum). (e) A representative image of a cell in a control matrix of collagen, with no embedded PNIPAAm microspheres at 37°C. (f) Cell-induced displacement ($|U|$) of the matrix shown in panel e. (g) A representative image of a cell in a PNIPAAm-embedded matrix of collagen at 37°C. (h) Cell-induced displacement ($|U|$) of the matrix shown in panel g. (i) The 80th percentile of the magnitude of displacement $|U|$ inside the dumbell-shaped regions (specified regions in panels e–h) were plotted for cells on control and contracted matrices. PNIPAAm-embedded matrices had significantly less deformation ($p = 0.0076$, rank sum), meaning that cellular activities (cell generated forces) were drastically reduced due to the softening of the contracted PNIPAAm-matrices. In panels c, d, and i, dots represent independent cells; lines indicate medians.

which was unexpected given that the contracting inclusions pull on the matrix fibers with tensile forces. We investigated the underlying mechanism behind the softening by studying the deformations undergone by the fibers, noting that the contracting inclusions also induced compressive strains, which led to buckling of the majority of the fibers within the matrix. By mapping the amount of fiber buckling to the extent of softening, we found that a greater extent of fiber buckling resulted in stronger softening. Lastly, we verified that this buckling-induced matrix softening was sufficient for cells to sense and respond with less elongated morphology and dramatically reduced force generation on the soft PNIPAAm-embedded matrices.

Prior work on the stiffness of collagen matrices typically used boundary conditions different than those in our study. Perhaps the most common are the boundary conditions of the commercial rheometer, which applies shear while simultaneously imposing additional constraints on the height and diameter of the matrices. Our rheometer experiments imposed these constraints with the additional condition of contracting inclusions, which produced local tensile forces within the matrix, thereby causing stiffening (Fig. 1). Our observation of stiffening induced by tensile forces is conceptually similar to observations of prior studies in which tensile forces were generated by uniaxial pretension [35, 37, 41] or via cell contraction [11, 12]. It is important to note that our experiments differed fundamentally from recent studies that introduced inclusions

in fibrous matrices and observed stiffening under uniaxial global compression [58, 59], because our study used inclusions at a lower concentration that contracted rather than being inert. Our findings are also distinct from the rheometer experiments showing that uniaxial global compression of a fibrous matrix leads to softening in shear [35, 37]. Although our simulations and experiments showed softening as well, they differed from the prior rheometer experiments, because the prior experiments applied only compressive forces to the matrix when observing softening. In our study, the contracting inclusions produced both tension and compression. Although tension would be expected to lead to strain stiffening, compression-induced buckling outweighed effects of stiffening for matrices with free boundaries, as evidenced by the matrix softening in both our model and experiments.

In both our modeling and experiments, the softening was observed when the external boundaries were free, allowing the matrix to shrink as a result of the contracting inclusions. Similar to our simulations and experiments, numerous prior experiments observing contraction of cell-embedded matrices used matrices with free boundaries, in which cell contraction caused global matrix shrinking [2, 20, 21]. Our findings would suggest that in the common experiment quantifying contraction of cell-embedded matrices, the stiffness decreases during contraction. Beyond these experiments, we expect our findings to apply to numerous other scenarios wherein the matrix is able to contract. In considering other applications of our findings, it is important to emphasize that most systems have boundaries that are neither fully free nor fully fixed but rather somewhere in between. Following our findings that the softening results from buckling which in turn results from contractile (negative) strain, our findings suggest softening would occur whenever the embedded inclusions (or cells) cause the matrix to shrink.

Our study elucidated that the buckled fibers played the pivotal role in softening the contracted PNIPAAm-embedded matrices at the scale of a cell. Over the last decade, fiber buckling has been found to have important effects on other mechanical phenomena. For example, buckling induced by the contractile forces of a cell dominantly contribute to long range transmission of cell-induced displacements within the matrix [22, 31, 50, 60, 61]. Interestingly, in long range displacement propagation, effects of fiber buckling supersede those of strain stiffening, which was initially thought to be the key contributor [62] and later found to be insufficient [63]. Fiber buckling also mediates a severe form of nonlinearity in the matrix that induces instabilities at the scale of the fibers leading to strong local densification, akin to a phase transition [5, 28]. Direct evidence for fiber buckling has been obtained from images in matrices under global uniaxial compression [59, 64], global shear [65], and local contraction of a single inclusion [22]. Here, substantial buckling occurred in a system with many contracting inclusions, which is interesting, given that the multiple inclusions supported tensile force chains connecting them, whereas buckling is an instability that occurs under compression. Our results pointed to a new role of fiber buckling, wherein the multiple contracting inclusions buckled the majority of fibers in the matrix. We directly related fiber buckling to softening in the 2D model by quantifying excess lengths as an indicator for buckling and showing that they correlated strongly with the amount of softening. The model predictions were confirmed by experiments, though the extent of softening in the experiments was less than in the 2D model (see Supplemental Note 1 for further discussion). In summary, the effects of buckling of fibers under compression outweighed the effects of stiffening of fibers under tension, causing softening in all directions. In future work, it would be interesting to study the effects of buckling in more complicated systems, such as composites of collagen fibers and hyaluronic acid, wherein fiber buckling is reduced [28].

Prior studies showed that individual contractile cells can locally pull on the matrix fibers, stiffening the matrix at scales of tens of microns. Experiments have measured stiffening near contracting cells in fibrous matrices to be as large as a factor of 10 [13–15]. However, a few recent nanoindentation and microrheometry experiments observed softening of matrices containing multiple contracting cells [16–18, 66], which is an apparent contradiction. The common resolution for this contradiction was to assume that the softening

was a consequence of matrix degradation due to cell-secreted metalloproteinases [17, 18]. It is important to identify other potential explanations for softening, however, because clinical trials using metalloproteinase inhibitors in the tumor microenvironment have so far been ineffective [67–69]. Our PNIPAAm-embedded matrices with contracting PNIPAAm microspheres mimicked the forces in these systems and exhibited similar matrix softening at cellular length scales with no chemical degradation present. Together, our experiments and simulations show that fiber buckling induced by the contractile forces of a cell is a potential mechanics-based explanation for the softening.

Our finding of contraction-induced softening raises new questions for investigation in future research. As an example, in wound healing, inflammatory response activates myofibroblast contraction and secretion of new matrix, but overly active myofibroblasts are undesirable as they create stiff fibrotic scars [70]. As myofibroblast activation is correlated to the matrix stiffness [71], it could be desirable for there to be matrix softening to suppress excessive myofibroblast activation, thereby minimizing excessive matrix production and contraction, and reducing the likelihood of scar formation. It would be interesting to determine whether the cell-induced softening found in our study plays a role in achieving homeostatic conditions following wounding. If cell-induced matrix softening has such an effect, a subsequent question is why such a mechanism is ineffective in other situations, such as the tumor microenvironment or progression of fibrotic disease, wherein it is commonly observed that the matrix stiffens rather than softens. These questions, which are enabled by our findings of contraction-induced softening, provide insightful new directions for investigation.

Acknowledgments

This work was supported by the National Science Foundation grant number CMMI-1749400 and the National Cancer Institute of the National Institutes of Health under award numbers R01CA179556 and U54CA268069 and University of Wisconsin Carbone Cancer Center Support Grant P30CA014520. We thank Lance Rodenkirch for his assistance in using the upright confocal microscope at the University of Wisconsin–Madison Optical Imaging Core (supported by the grant number 1S10OD025040-01).

Declarations

Conflicts of Interest

The authors have no conflicts of interest to declare.

References

[1] L. D. Muiznieks, F. W. Keeley, Molecular assembly and mechanical properties of the extracellular matrix: A fibrous protein perspective, BBA-Mol Basis Dis 1832 (7) (2013) 866–875.

[2] E. Bell, B. Ivarsson, C. Merrill, Production of a tissue-like structure by contraction of collagen lattices by human fibroblasts of different proliferative potential in vitro., P Natl Acad Sci USA 76 (3) (1979) 1274–1278.

[3] L. K. Wrobel, T. R. Fray, J. E. Molloy, J. J. Adams, M. P. Armitage, J. C. Sparrow, Contractility of single human dermal myofibroblasts and fibroblasts, Cell Motil Cytoskel 52 (2) (2002) 82–90.

[4] P. Lu, K. Takai, V. M. Weaver, Z. Werb, Extracellular matrix degradation and remodeling in development and disease, CSH Perspect Biol 3 (12) (2011) a005058.

[5] G. Grekas, M. Proestaki, P. Rosakis, J. Notbohm, C. Makridakis, G. Ravichandran, Cells exploit a phase transition to mechanically remodel the fibrous extracellular matrix, J R Soc Interface 18 (175) (2021) 20200823.

[6] V. Vogel, M. Sheetz, Local force and geometry sensing regulate cell functions, Nat Rev Mol Cell Bio 7 (4) (2006) 265–275.

[7] M. S. Hall, F. Alisafaei, E. Ban, X. Feng, C.-Y. Hui, V. B. Shenoy, M. Wu, Fibrous nonlinear elasticity enables positive mechanical feedback between cells and ECMs, P Natl Acad Sci USA 113 (49) (2016) 14043–14048.

[8] J. Tao, S. X. Sun, Active biochemical regulation of cell volume and a simple model of cell tension response, Biophys J 109 (8) (2015) 1541–1550.

[9] M. P. Murrell, R. Voituriez, J.-F. Joanny, P. Nassoy, C. Sykes, M. L. Gardel, Liposome adhesion generates traction stress, Nat Phys 10 (2) (2014) 163–169.

[10] Y. Wu, M. R. Zanotelli, J. Zhang, C. A. Reinhart-King, Matrix-driven changes in metabolism support cytoskeletal activity to promote cell migration, Biophys J 120 (9) (2021) 1705–1717.

[11] S. F. Schlick, F. Spreckelsen, M. Tiburcy, L. M. Iyer, T. Meyer, L. C. Zelarayan, S. Luther, U. Parlitz, W.-H. Zimmermann, F. Rehfeldt, Agonistic and antagonistic roles of fibroblasts and cardiomyocytes on viscoelastic stiffening of engineered human myocardium, Prog Biophys Mol Bio 144 (2019) 51–60.

[12] K. A. Jansen, R. G. Bacabac, I. K. Piechocka, G. H. Koenderink, Cells actively stiffen fibrin networks by generating contractile stress, Biophys J 105 (10) (2013) 2240–2251.

[13] H. Yang, E. Berthier, C. Li, P. Ronceray, Y. L. Han, C. P. Broedersz, S. Cai, M. Guo, Local response and emerging nonlinear elastic length scale in biopolymer matrices, P Natl Acad Sci USA 120 (23) (2023) e2304666120.

[14] Y. L. Han, P. Ronceray, G. Xu, A. Malandrino, R. D. Kamm, M. Lenz, C. P. Broedersz, M. Guo, Cell contraction induces long-ranged stress stiffening in the extracellular matrix, P Natl Acad Sci USA 115 (16) (2018) 4075–4080.

[15] A. Jagiełło, M. Lim, E. Botvinick, Dermal fibroblasts and triple-negative mammary epithelial cancer cells differentially stiffen their local matrix, APL Bioeng 4 (4).

[16] P. K. Viji Babu, C. Rianna, U. Mirastschijski, M. Radmacher, Nano-mechanical mapping of interdependent cell and ECM mechanics by AFM force spectroscopy, Sci Rep 9 (2019) 12317.

[17] J. Pokki, I. Zisi, E. Schulman, D. Indana, O. Chaudhuri, Magnetic probe-based microrheology reveals local softening and stiffening of 3d collagen matrices by fibroblasts, Biomed Microdevices 23 (2) (2021) 27.

[18] J. Hafner, D. Grijalva, A. Ludwig-Husemann, S. Bertels, L. Bensinger, A. Raic, J. Gebauer, C. Oelschlaeger, M. Bastmeyer, K. Bieback, C. Lee-Thedieck, N. Willenbacher, Monitoring matrix remodeling in the cellular microenvironment using microrheology for complex cellular systems, Acta Biomater 111 (2020) 254–266.

[19] S. Natan, Y. Koren, O. Shelah, S. Goren, A. Lesman, Long-range mechanical coupling of cells in 3d fibrin gels, Mol Biol Cell 31 (14) (2020) 1474–1485.

[20] U. Doha, O. Aydin, M. S. H. Joy, B. Emon, W. Drennan, M. T. A. Saif, Disorder to order transition in cell-ECM systems mediated by cell-cell collective interactions, Acta Biomater 154 (2022) 290–301.

[21] P. Fernandez, A. R. Bausch, The compaction of gels by cells: a case of collective mechanical activity, Integr Biol 1 (3) (2009) 252–259.

[22] B. Burkel, J. Notbohm, Mechanical response of collagen networks to nonuniform microscale loads, Soft Matter 13 (34) (2017) 5749–5758.

[23] M. Proestaki, A. Ogren, B. Burkel, J. Notbohm, Modulus of fibrous collagen at the length scale of a cell, Exp Mech 59 (9) (2019) 1323–1334.

[24] E. Bar-Kochba, J. Toyjanova, E. Andrews, K.-S. Kim, C. Franck, A fast iterative digital volume correlation algorithm for large deformations, Exp Mech 55 (1) (2015) 261–274.

[25] J. M. Szulczewski, D. R. Inman, M. Proestaki, J. Notbohm, B. M. Burkel, S. M. Ponik, Directional cues in the tumor microenvironment due to cell contraction against aligned collagen fibers, Acta Biomater 129 (2021) 96–109.

[26] B. Burkel, M. Proestaki, S. Tyznik, J. Notbohm, Heterogeneity and nonaffinity of cell-induced matrix displacements, Phys Rev E 98 (5) (2018) 052410.

[27] M. Proestaki, B. Burkel, E. E. Galles, S. M. Ponik, J. Notbohm, Effect of matrix heterogeneity on cell mechanosensing, Soft Matter 17 (2021) 10263–10273.

[28] M. Proestaki, M. Sarkar, B. M. Burkel, S. M. Ponik, J. Notbohm, Effect of hyaluronic acid on microscale deformations of collagen gels, J Mech Behav Biomed 135 (2022) 105465.

[29] S. B. Lindström, D. A. Vader, A. Kulachenko, D. A. Weitz, Biopolymer network geometries: Characterization, regeneration, and elastic properties, Phys Rev E 82 (5) (2010) 051905.

[30] S. B. Lindström, A. Kulachenko, L. M. Jawerth, D. A. Vader, Finite-strain, finite-size mechanics of rigidly cross-linked biopolymer networks, Soft Matter 9 (30) (2013) 7302–7313.

[31] P. Grimmer, J. Notbohm, Displacement propagation in fibrous networks due to local contraction, J Biomech Eng—T ASME 140 (4) (2018) 041011.

[32] S. Arzash, J. L. Shivers, A. J. Licup, A. Sharma, F. C. MacKintosh, Stress-stabilized subisostatic fiber networks in a ropelike limit, Phys Rev E 99 (4) (2019) 042412.

[33] A. M. Stein, D. A. Vader, L. M. Jawerth, D. A. Weitz, L. M. Sander, An algorithm for extracting the network geometry of three-dimensional collagen gels, J Microsc-Oxford 232 (3) (2008) 463–475.

[34] A. J. Licup, S. Münster, A. Sharma, M. Sheinman, L. M. Jawerth, B. Fabry, D. A. Weitz, F. C. MacKintosh, Stress controls the mechanics of collagen networks, P Natl Acad Sci USA 112 (31) (2015) 9573–9578.

[35] M. Vahabi, A. Sharma, A. J. Licup, A. S. Van Oosten, P. A. Galie, P. A. Janmey, F. C. MacKintosh, Elasticity of fibrous networks under uniaxial prestress, Soft matter 12 (22) (2016) 5050–5060.

[36] J. Feng, H. Levine, X. Mao, L. M. Sander, Alignment and nonlinear elasticity in biopolymer gels, Phys Rev E 91 (4) (2015) 042710.

[37] A. S. Van Oosten, M. Vahabi, A. J. Licup, A. Sharma, P. A. Galie, F. C. MacKintosh, P. A. Janmey, Uncoupling shear and uniaxial elastic moduli of semiflexible biopolymer networks: compression-softening and stretch-stiffening, Sci Rep 6 (2016) 19270.

[38] M. Sarkar, J. Notbohm, Quantification of errors in applying dic to fiber networks imaged by confocal microscopy, Exp Mech 62 (7) (2022) 1175–1189.

[39] M. Sarkar, J. Notbohm, Evolution of force chains explains the onset of strain stiffening in fiber networks, J Appl Mech 89 (11) (2022) 111008.

[40] E. Ban, H. Wang, J. M. Franklin, J. T. Liphardt, P. A. Janmey, V. B. Shenoy, Strong triaxial coupling and anomalous poisson effect in collagen networks, P Natl Acad Sci USA 116 (14) (2019) 6790–6799.

[41] H. Hatami-Marbini, M. Rohanifar, Nonlinear mechanical properties of prestressed branched fibrous networks, Biophys J 120 (3) (2021) 527–538.

[42] S. Adam, A. Mohanan, S. Bakshi, A. Ghadai, S. Majumdar, Network architecture dependent mechanical response in temperature responsive collagen-pnipam composites, Colloid Surface B 227 (2023) 113380.

[43] M. A. Kotlarchyk, S. G. Shreim, M. B. Alvarez-Elizondo, L. C. Estrada, R. Singh, L. Valdevit, E. Kniazeva, E. Gratton, A. J. Putnam, E. L. Botvinick, Concentration independent modulation of local micromechanics in a fibrin gel, Plos One 6 (5) (2011) e20201.

[44] C. A. Jones, M. Cibula, J. Feng, E. A. Krnacik, D. H. McIntyre, H. Levine, B. Sun, Micromechanics of cellularized biopolymer networks, P Natl Acad Sci USA 112 (37) (2015) E5117–E5122.

[45] S. Van Helvert, P. Friedl, Strain stiffening of fibrillar collagen during individual and collective cell migration identified by afm nanoindentation, ACS Appl Mater Inter 8 (34) (2016) 21946–21955.

[46] T. Fischer, A. Hayn, C. T. Mierke, Effect of nuclear stiffness on cell mechanics and migration of human breast cancer cells, Front Cell Dev Biol 8 (2020) 393.

[47] A. Mann, R. S. Sopher, S. Goren, O. Shelah, O. Tchaicheeyan, A. Lesman, Force chains in cell–cell mechanical communication, J R Soc Interface 16 (159) (2019) 20190348.

[48] J. Ruiz-Franco, J. van Der Gucht, Force transmission in disordered fibre networks, Front Cell Dev Biol 10 (2022) 931776.

[49] A. J. Licup, A. Sharma, F. C. MacKintosh, Elastic regimes of subisostatic athermal fiber networks, Phys Rev E 93 (1) (2016) 012407.

[50] J. Notbohm, A. Lesman, P. Rosakis, D. A. Tirrell, G. Ravichandran, Microbuckling of fibrin provides a mechanism for cell mechanosensing, J R Soc Interface 12 (108) (2015) 20150320.

[51] D. Humphries, J. Grogan, E. Gaffney, Mechanical cell–cell communication in fibrous networks: the importance of network geometry, Bull Math Biol 79 (2017) 498–524.

[52] R. S. Sopher, H. Tokash, S. Natan, M. Sharabi, O. Shelah, O. Tchaicheeyan, A. Lesman, Nonlinear elasticity of the ecm fibers facilitates efficient intercellular communication, Biophys J 115 (7) (2018) 1357–1370.

[53] E. Ban, J. M. Franklin, S. Nam, L. R. Smith, H. Wang, R. G. Wells, O. Chaudhuri, J. T. Liphardt, V. B. Shenoy, Mechanisms of plastic deformation in collagen networks induced by cellular forces, Biophys J 114 (2) (2018) 450–461.

[54] D. Lee, M. M. Rahman, Y. Zhou, S. Ryu, Three-dimensional confocal microscopy indentation method for hydrogel elasticity measurement, Langmuir 31 (35) (2015) 9684–9693.

[55] J. Merson, N. Parvez, R. Picu, Probing soft fibrous materials by indentation, Acta Biomater 163 (2023) 25–34.

[56] J. Sapudom, L. Kalbitzer, X. Wu, S. Martin, K. Kroy, T. Pompe, Fibril bending stiffness of 3d collagen matrices instructs spreading and clustering of invasive and non-invasive breast cancer cells, Biomaterials 193 (2019) 47–57.

[57] V. S. Rozova, A. G. Anwer, A. E. Guller, H. A. Es, Z. Khabir, A. I. Sokolova, M. U. Gavrilov, E. M. Goldys, M. E. Warkiani, J. P. Thiery, A. V. Zvyagin, Machine learning reveals mesenchymal breast carcinoma cell adaptation in response to matrix stiffness, Plos Comput Biol 17 (7) (2021) e1009193.

[58] A. S. van Oosten, X. Chen, L. Chin, K. Cruz, A. E. Patteson, K. Pogoda, V. B. Shenoy, P. A. Janmey, Emergence of tissue-like mechanics from fibrous networks confined by close-packed cells, Nature 573 (7772) (2019) 96–101.

[59] J. L. Shivers, J. Feng, A. S. van Oosten, H. Levine, P. A. Janmey, F. C. MacKintosh, Compression stiffening of fibrous networks with stiff inclusions, P Natl Acad Sci USA 117 (35) (2020) 21037–21044.

[60] P. Rosakis, J. Notbohm, G. Ravichandran, A model for compression-weakening materials and the elastic fields due to contractile cells, J Mech Phys Solids 85 (2015) 16–32.

[61] S. Goren, Y. Koren, X. Xu, A. Lesman, Elastic anisotropy governs the range of cell-induced displacements, Biophys J 118 (5) (2020) 1152–1164.

[62] J. P. Winer, S. Oake, P. A. Janmey, Non-linear elasticity of extracellular matrices enables contractile cells to communicate local position and orientation, Plos One 4 (7) (2009) e6382.

[63] M. S. Rudnicki, H. A. Cirka, M. Aghvami, E. A. Sander, Q. Wen, K. L. Billiar, Nonlinear strain stiffening is not sufficient to explain how far cells can feel on fibrous protein gels, Biophys J 105 (1) (2013) 11–20.

[64] O. V. Kim, R. I. Litvinov, J. W. Weisel, M. S. Alber, Structural basis for the nonlinear mechanics of fibrin networks under compression, Biomaterials 35 (25) (2014) 6739–6749.

[65] S. Münster, L. M. Jawerth, B. A. Leslie, J. I. Weitz, B. Fabry, D. A. Weitz, Strain history dependence of the nonlinear stress response of fibrin and collagen networks, P Natl Acad Sci USA 110 (30) (2013) 12197–12202.

[66] A. Glentis, P. Oertle, P. Mariani, A. Chikina, F. El Marjou, Y. Attieh, F. Zaccarini, M. Lae, D. Loew, F. Dingli, P. Sirven, M. Schoumacher, B. G. Gurchenkov, M. Plodinec, D. M. Vignjevic, Cancer-associated fibroblasts induce metalloprotease-independent cancer cell invasion of the basement membrane, Nature Commun 8 (1) (2017) 924.

[67] T. Liu, L. Zhou, D. Li, T. Andl, Y. Zhang, Cancer-associated fibroblasts build and secure the tumor microenvironment, Front Cell Dev Biol 7 (2019) 60.

[68] F. Kai, A. P. Drain, V. M. Weaver, The extracellular matrix modulates the metastatic journey, Dev Cell 49 (3) (2019) 332–346.

[69] A. Saraswathibhatla, D. Indana, O. Chaudhuri, Cell–extracellular matrix mechanotransduction in 3d, Nat Rev Mol Cell Bio 24 (7) (2023) 495—516.

[70] L. Moretti, J. Stalfort, T. H. Barker, D. Abebayehu, The interplay of fibroblasts, the extracellular matrix, and inflammation in scar formation, J Biol Chem 298 (2).

[71] B. Hinz, The myofibroblast: paradigm for a mechanically active cell, J Biomech 43 (1) (2010) 146–155.

Supplemental Information

Unexpected softening of a fibrous matrix by contracting inclusions

Mainak Sarkar,[a] Brian M. Burkel,[b,c] Suzanne M. Ponik,[b,c] Jacob Notbohm[a,c,*]

[a] Department of Mechanical Engineering, University of Wisconsin–Madison, Madison, WI, USA
[b] Department of Cell and Regenerative Biology, University of Wisconsin–Madison, Madison, WI, USA
[c] University of Wisconsin Carbone Cancer Center, Madison, WI, USA
[*] Corresponding author: Jacob Notbohm, jknotbohm@wisc.edu

Supplemental Figures

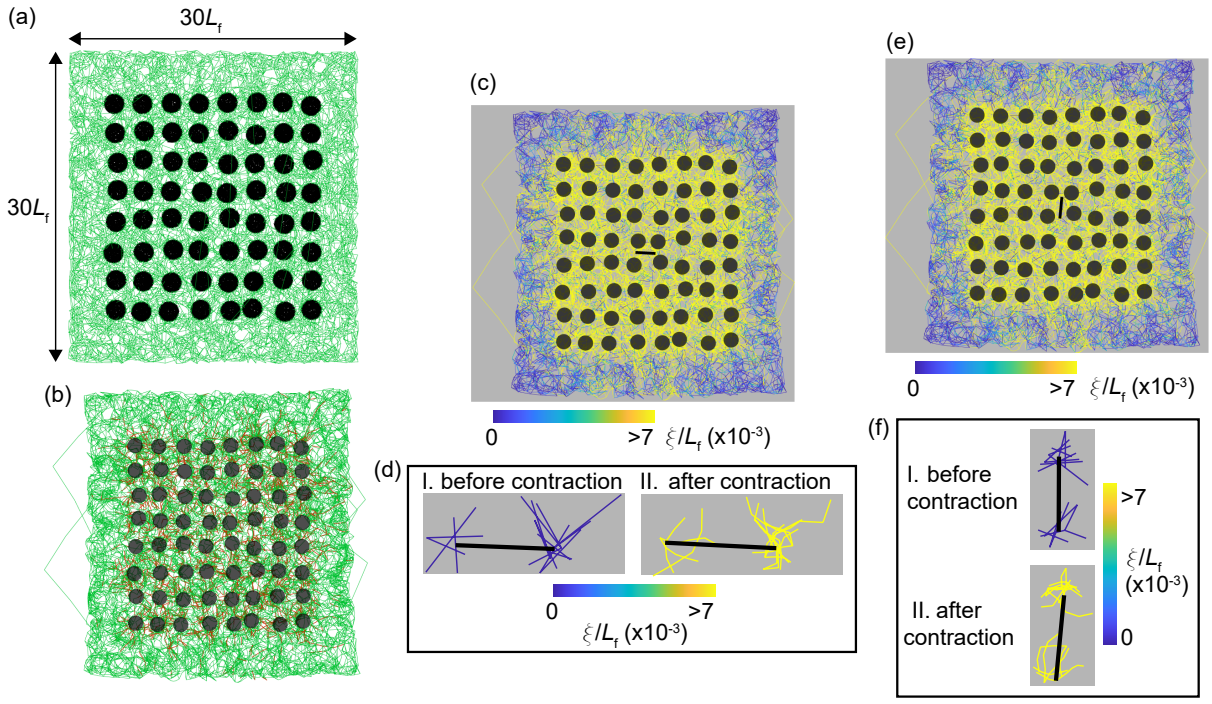

Figure S1. Simulations on a second independent matrix model with a group of contracting inclusions. (a) The undeformed state of the matrix. The inclusions had a diameter of $D = 2L_f$ and were randomly embedded inside the matrix at an average inter-inclusion spacing of $\approx 1.5L_f$. (b) After inclusions contracted by 40%, force transmission is mapped by force chains constituting the top 20% highly stretched fibers in the matrix (red). These force chains emanated radially from the periphery of the inclusions. (c) The fibers of the deformed matrix are color coded based on their values of normalized excess length (ξ/L_f). The contracting dipole (black line in the inter-inclusion space) registers the stiffness of the matrix. (d) Enlarged view of the dipole with the matrix fibers in its close vicinity before (I) and after (II) contraction of the inclusions. In II, the fibers are highly buckled with large excess lengths. The fibers constituting the microenvironment of the dipole were identified using the technique described in Figs. 3 & 4. (e, f) A differently aligned dipole was considered in the matrix (e) and the excess lengths of fibers in the dipole's microenvironment were mapped (f) before and after the contraction of inclusions, similar to panels c and d.

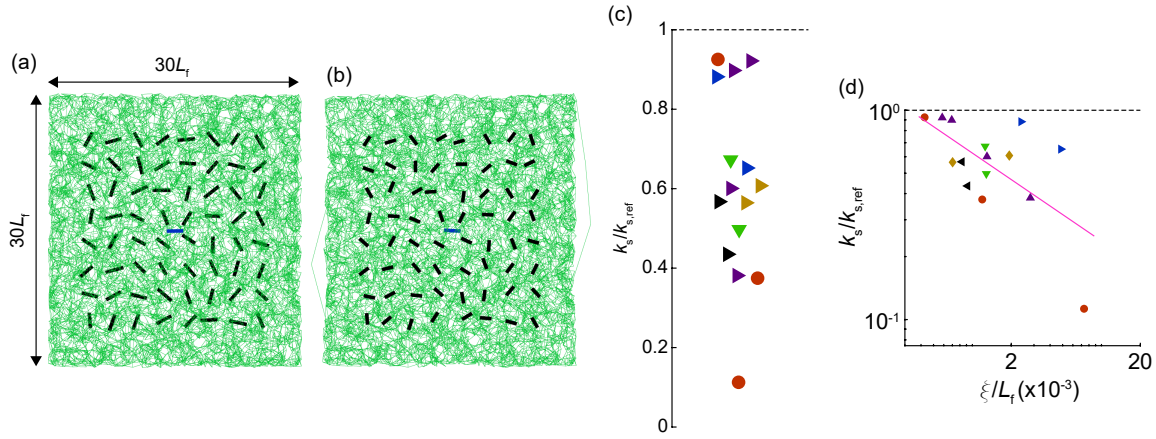

Figure S2. Softening in fibrous matrix due to contracting dipoles. (a) Uncontracted matrix with randomly embedded dipoles instead of circular inclusions. The central dipole highlighted in blue measured the stiffness of the uncontracted matrix ($k_{s,ref}$). (b) Contracted matrix due to the axial contraction of the embedded dipoles. The dipoles were axially contracted by 40%. The central dipole highlighted in blue measured the stiffness of the contracted matrix (k_s). (c) The ratios $k_s/k_{s,ref}$ for differently aligned dipoles in six independent matrices were consistently less than one, indicating softening in the matrix in all directions, similar to the results of the inclusion-matrix system shown in Fig. 2. (d) Scatter plot of normalized stiffness ($k_s/k_{s,ref}$) sensed by each dipole against average excess length (ξ/L_f) in the vicinity of that dipole. The correlation between the reduction in matrix stiffness and excess lengths was statistically significant ($p = 0.03$, Pearson). In panels c and d, each marker type indicates a dipole from an independent fiber network model.

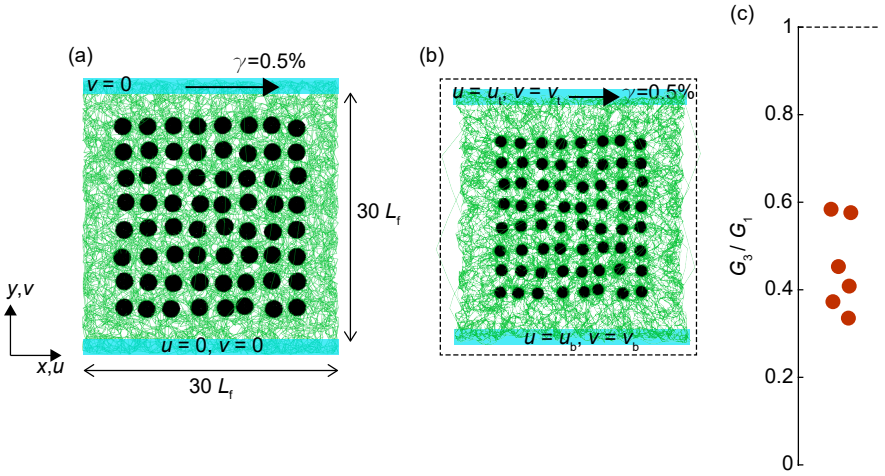

Figure S3. Effect of contracting inclusions on matrix softening in simple shear. (a) Matrix with uncontracted inclusions subjected to global simple shear $\gamma = 0.5\%$. The small strain linear shear modulus of the uncontracted matrix was defined as G_1. The simple shear boundary condition was applied to the nodes at the top and bottom of the matrix (highlighted in blue). (b) Matrix with contracted inclusions subjected to global simple shear $\gamma = 0.5\%$. The simulation was performed in two steps. In the first step, the inclusions contracted with free boundary conditions allowing the matrix to globally contract from its reference state (dashed rectangle shows the initial size of the matrix). In the second step, the positions of the nodes at the top and bottom boundaries (highlighted in blue) were used as the reference state for imposing simple shear. The small strain linear shear modulus of the contracted matrix was defined as G_3. (c) The ratios G_3/G_1 for six independent matrices were less than one indicating global softening of the contracted matrices.

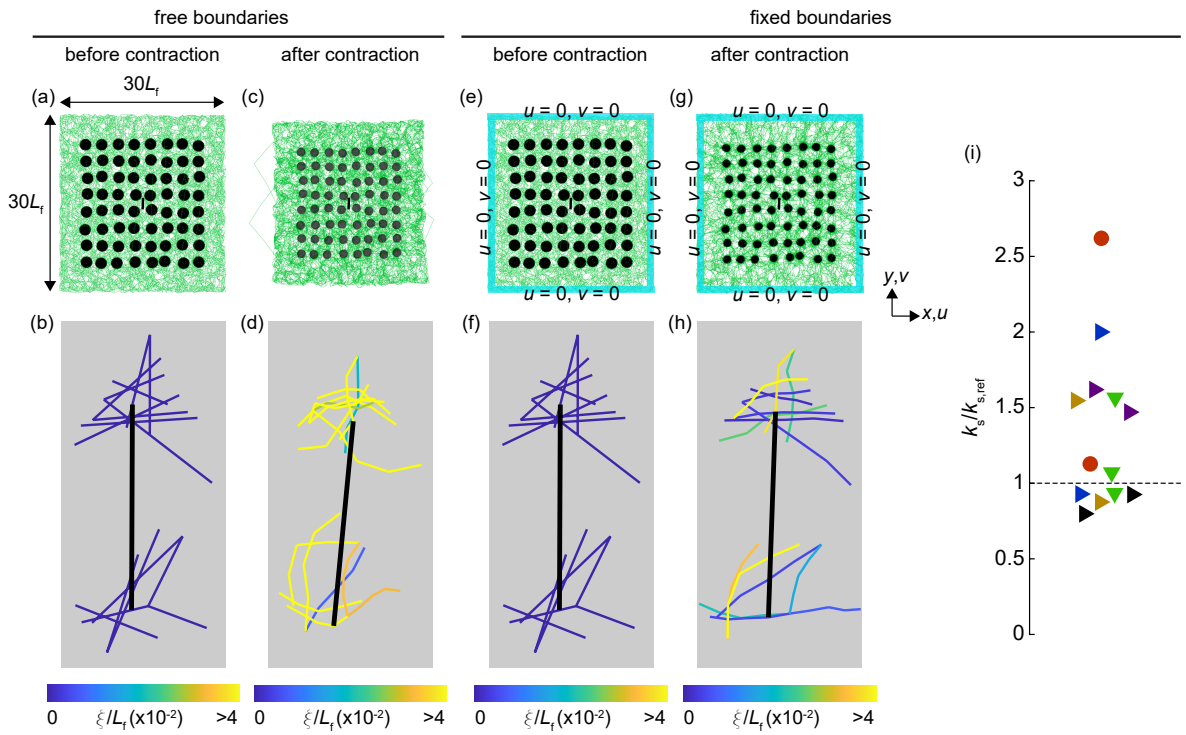

Figure S4. Effect of contracting inclusions in matrices with fixed boundaries. (a) Image of an uncontracted matrix with multiple inclusions, with the outer boundaries of the matrix free. The dipole used to measure stiffness is marked by the black solid line. (b) Excess lengths of the fibers in the close vicinity of the dipole in the uncontracted matrix of panel a. The fibers were straight before the contraction of inclusions. (c) Image of the matrix from panel a after contraction of the inclusions. The matrix was allowed to contract without constraining the outer boundaries. The dipole used to measure stiffness is marked by the black solid line. (d) The fibers near the dipole of the contracted matrix of panel c showed strong buckling, as indicated by large values of the normalized fiber excess lengths (ξ/L_f). (e) Image of an uncontracted matrix with multiple inclusions, with the nodes near the outer boundaries of the matrix fixed (highlighted in blue). The dipole used to measure stiffness is marked by the black solid line. (f) Excess lengths of the fibers near the dipole of the uncontracted matrix of panel e. (g) Image of the matrix from panel e after contraction of the inclusions. As in panel e, nodes at the outer boundaries (highlighted in blue) were fixed. The dipole used to measure stiffness is marked by the black solid line. (h) Excess lengths of the fibers near the dipole of the deformed matrix of panel g. The fibers showed modest buckling compared to panel d, indicating the boundaries largely suppressed buckling. (i) For differently aligned dipoles and for six independent matrices with fixed boundaries, the ratio of the values of stiffness of the matrix sensed by the dipole after and before contraction of inclusions ($k_s/k_{s,ref}$) was recorded. Each marker indicates a different dipole; each marker shape indicates a different matrix.

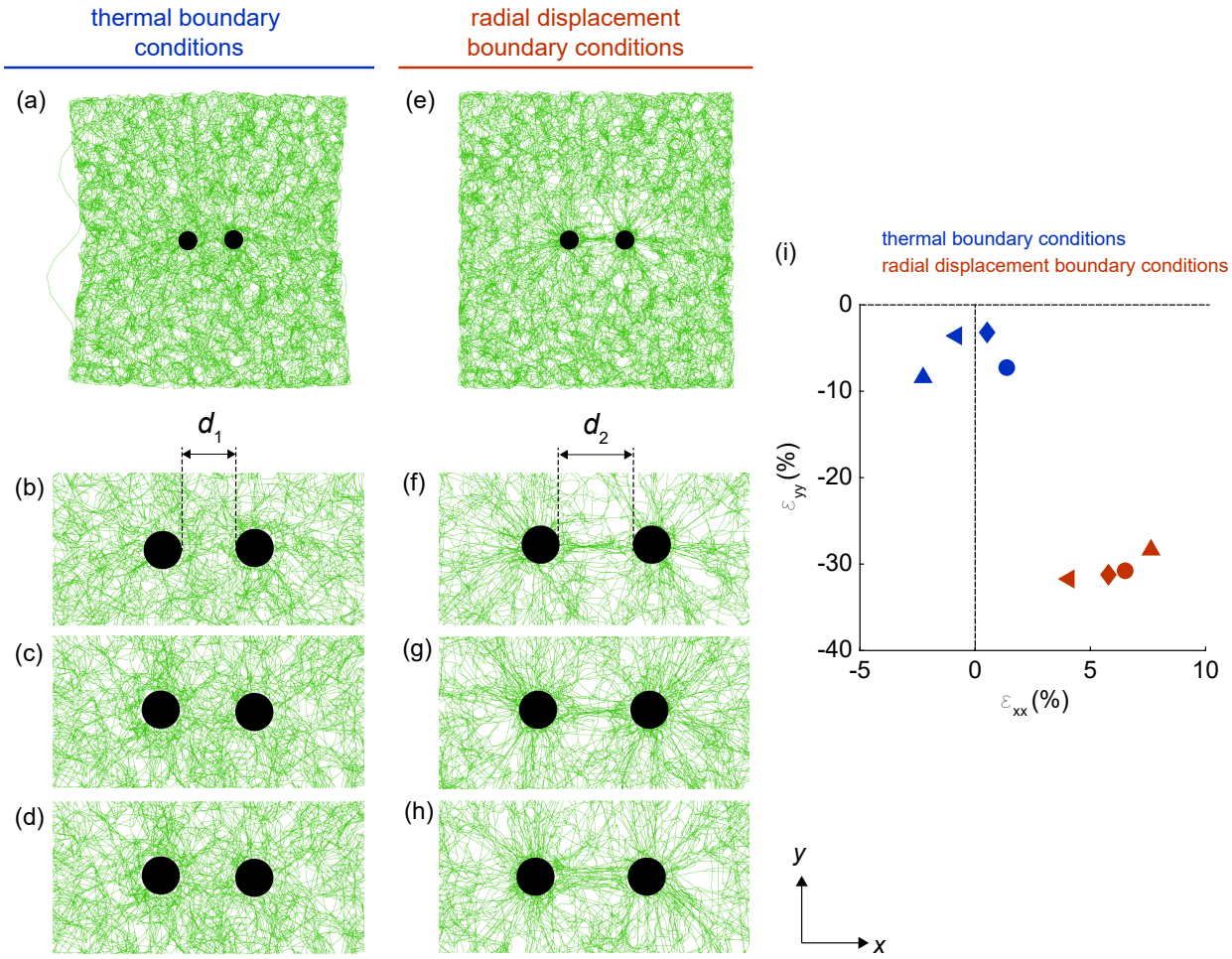

Figure S5. Subtle intricacies in modeling a matrix with contracting inclusions. (a) Deformed matrix with two contracted inclusions, where the inclusions were elastic bodies subjected to thermal radial contraction of 70%. In this system, both force equilibrium of the inclusions and kinematic compatibility of the matrix are ensured. The matrix had free outer boundaries. (b) Zoomed-in view of the deformed matrix of panel a. The separation distance between the inclusions, d_1, decreased as the inclusions thermally contracted. (c, d) Zoomed-in views of the deformed configurations of two other random matrices, with similar values of the shortened separation distance d_1 as that of panel b. In panels a–d, the inclusions were subjected to thermal boundary conditions. (e) Deformed matrix with two contracted inclusions, where the nodes at the boundary of each inclusion were subjected to inward radial displacement to impose a radial contraction of 70%. In this system, force equilibrium of the inclusions is not required. The matrix had free outer boundaries. (f) Zoomed-in view of the deformed matrix of panel e. The fibers were strongly densified and aligned between the inclusions. Note that the separation distance between the inclusions (d_2) did not decrease as the inclusions contracted, *i.e.*, $d_2 > d_1$. (g, h) Zoomed-in views of the deformed configurations of two other random matrices, similarly depicting densification between the inclusions, as in panel f. In panels e–h, the inclusions were subjected to radial displacement boundary conditions. (i) For four independent matrix models, the normal strains were quantified in the region between the contracting inclusions in directions parallel to and transverse to the axis connecting the inclusions, ε_{xx} and ε_{yy}, respectively. When the inclusions were thermally contracted, ε_{xx} was close to zero (occasionally negative) and ε_{yy} had small negative values. In contrast, when the inclusions were subjected to displacement boundary conditions, $\varepsilon_{xx} > 0$ and ε_{yy} was strongly negative, indicating strong fiber alignment and densification. Each marker shape indicates an independent fiber network model.

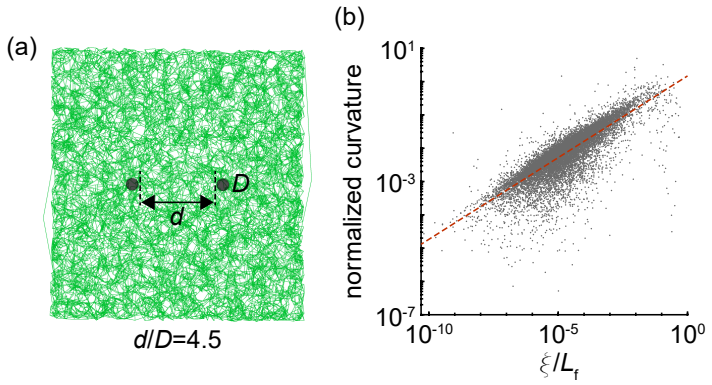

Figure S6. Correlation between curvature and excess length of fibers in a deformed matrix. (a) A representative deformed matrix with two contracted inclusions. (b) The values of the normalized curvature of all of the fibers in the matrix were plotted against their normalized excess lengths (ξ/L_f), with the data exhibiting a clear positive correlation.

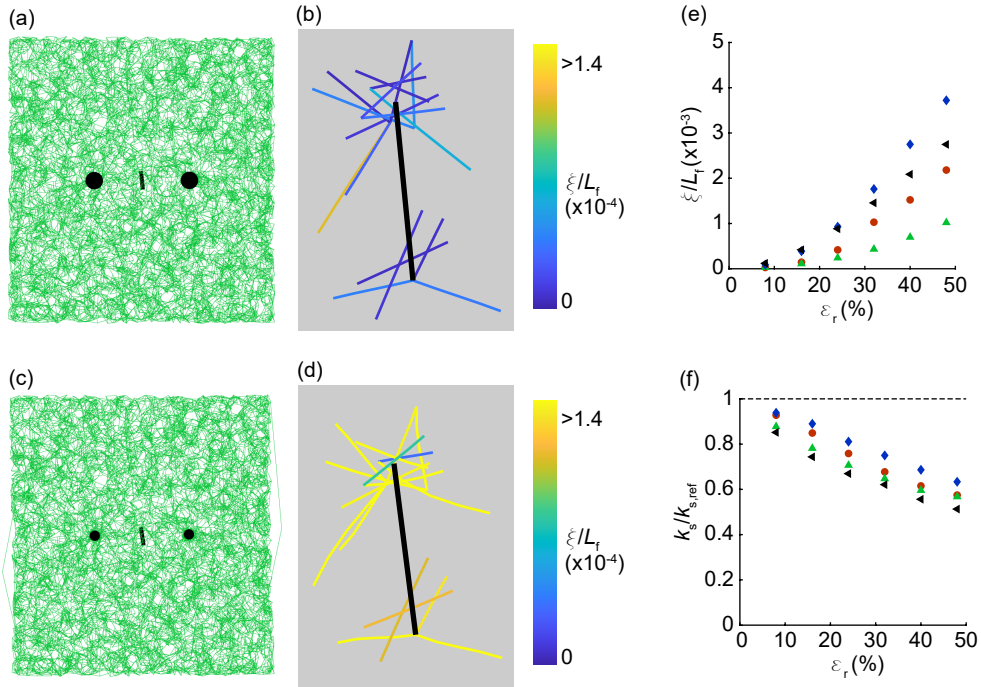

Figure S7. Effect of magnitude of radial contraction on softening. Models were embedded with two inclusions of diameter $D = 2L_f$, separated by inter-inclusion spacing d, with $d/D = 4.5$. Nominal radial contractile strain of the inclusions, ε_r, ranged from 8% to 48%. (a) Image showing the deformed matrix where the inclusions were radially contracted by $\varepsilon_r = 8\%$. The central dipole of length $2L_f$ is perpendicular to the imaginary line joining the centers of the inclusions. (b) Enlarged view of the central dipole of panel a with fibers in its vicinity color coded by the values of their excess lengths. (c) Image showing the deformed matrix where the inclusions were radially contracted by $\varepsilon_r = 48\%$. The central dipole of length $2L_f$ is perpendicular to the imaginary line joining the centers of the inclusions. (d) Enlarged view of the central dipole of panel c with fibers in its vicinity color coded by the values of their excess lengths. A comparison of panels b and d indicates considerable increase in fiber buckling in panel d due to the increase in the radial

contraction of the inclusions from $\varepsilon_r = 8\%$ to $\varepsilon_r = 48\%$. (e) Plot showing the dependence of the average excess length of fibers (ξ/L_f) in the microenvironment of the dipole on the radial contraction of the inclusions ε_r. (f) The normalized stiffness of the matrix in the vicinity of the transverse dipole ($k_s/k_{s,ref}$) decreased approximately linearly with the radial contraction of the inclusions ε_r. In panels e and f, each marker color indicates an independent fiber network model.

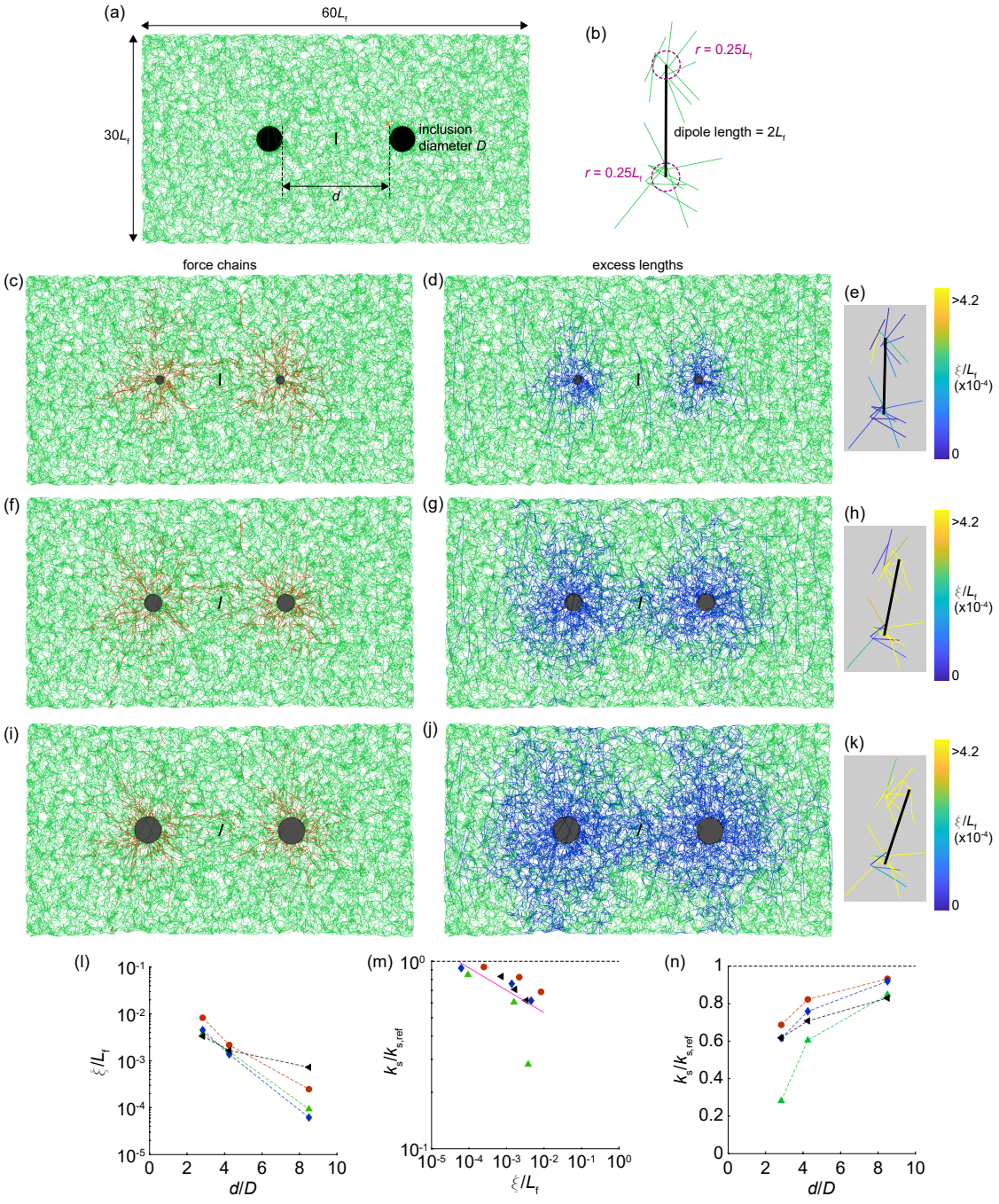

Figure S8. Simulations on matrix models containing two contracting inclusions of varying diameter. (a) A representative matrix model containing two inclusions of diameter D, separated by $d = 17L_f$. The central dipole of length $2L_f$ is transverse to the imaginary line joining the centers of the inclusions. The inclusions

were radially contracted by 40%. (b) Enlarged view of the central dipole, which contracts to sense the stiffness of the matrix. Fibers shown pass through the circular regions of radius $0.25L_f$ centered at the fiber's end points and define the microenvironment of the dipole. (c) A representative deformed state of the matrix with inclusion diameter $D = 2L_f$, with force chains highlighted red. These force chains consisted of the 5% most stretched fibers, and they emanated radially from the periphery of the contracted inclusions. (d) A representative deformed state of the matrix with inclusion diameter $D = 2L_f$, with the 5% most buckled fibers highlighted blue. Buckled fibers primarily remained circumferential to the contracted inclusions. (e) The dipole of the system described in panels c and d. The matrix fibers in its microenvironment are colored based on the values of their excess lengths. (f, g, h) A representative deformed state of the matrix with inclusion diameter $D = 4L_f$, showing 5% most stretched fibers (f), the 5% most buckled fibers (g), and the zoomed-in view of the dipole with its microenvironment (h), similar to panels c–e. (i, j, k) A representative deformed state of the matrix with inclusion diameter $D = 6L_f$, showing the 5% most stretched fibers (i), the 5% most buckled fibers (j), and the zoomed-in view of the dipole with its microenvironment (k), similar to panels c–e. (l) Plot showing the dependence of the average excess length of fibers in the microenvironment of the dipole to the model parameter d/D. (m) Normalized stiffness of the matrix ($k_s/k_{s,ref}$) in the vicinity of transversely-oriented dipoles after contraction of the inclusions are always < 1 indicating softening. These data are also negatively correlated to the average excess length of fibers in the microenvironment of the dipole. (n) As a consequence of relations in panels l and m, the normalized stiffness of the matrix ($k_s/k_{s,ref}$) monotonically increases with the model parameter d/D. In panels l–n, each marker color indicates an independent fiber network model.

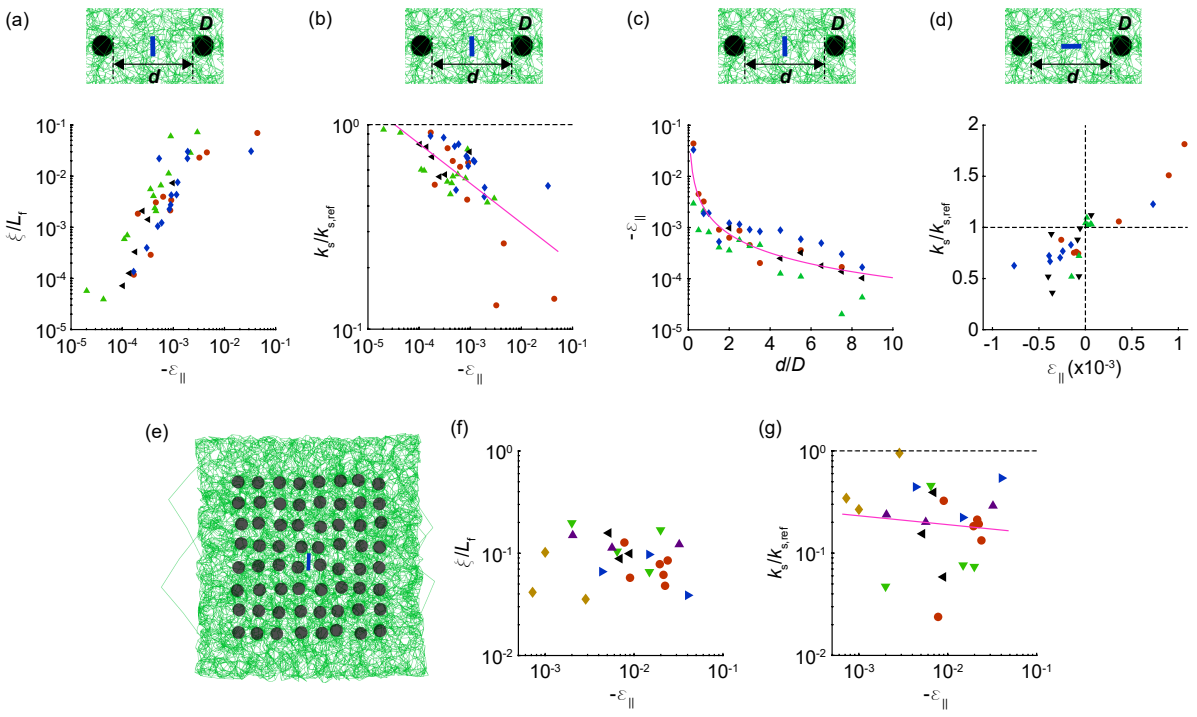

Figure S9. The extent of fiber buckling and softening is related to the the normal strain parallel to the dipole. (a) Plot showing dependence of average excess lengths of fibers in the microenvironment of each dipole to the contractile normal strain in the matrix parallel to the dipole ($-\varepsilon_{||}$). (b) Dependence of the normalized stiffness of the matrix ($k_s/k_{s,ref}$) in the vicinity of each dipole to the contractile normal strain in the matrix parallel to the dipole ($-\varepsilon_{||}$). (c) Contractile normal strain ($-\varepsilon_{||}$) plotted against the dimensionless inter-inclusion spacing d/D. Panels a–c correspond to models of matrices with two contracting inclusions and transversely aligned dipoles. (d) For the dipoles aligned parallel to the center line joining the two

contracting inclusions (inset), the plot shows the dependence of the normalized matrix stiffness ($k_s/k_{s,ref}$) in the vicinity of each dipole to the normal strain in the matrix parallel to the dipole ($\varepsilon_{||}$). Note that the matrix softens when $\varepsilon_{||} < 0$ and stiffens when $\varepsilon_{||} > 0$. The stochasticity leading to the frequent (and surprising) occurrence of softening in the matrix as described in Fig. 4p can be explained by the sign of the normal strain parallel to the dipole, $\varepsilon_{||}$. In panels a–d, each marker indicates an independent dipole, and each color indicates an independent fiber network model. (e) The matrix with many contracting inclusions considered in our study, where differently aligned dipoles (highlighted blue) measured the stiffness of the matrix. (f) For multi-inclusion matrices, as in panel e, plot of excess lengths of fibers in the microenvironment of each dipole against the contractile normal strain in the matrix parallel to the dipole ($-\varepsilon_{||}$). (g) For multi-inclusion matrices, plot of the stiffness ratio ($k_s/k_{s,ref}$) against $\varepsilon_{||}$. The correlations in panels f and g are weaker than a and b, which likely results from the complexity of the multi-inclusion matrices. Despite that the correlations were less strong in panels f and g, the broad observation that negative strain occurred along with fiber buckling and softening remained consistent. In panels f–g, each marker indicates a dipole at a different location, and each color indicates an independent fiber network model.

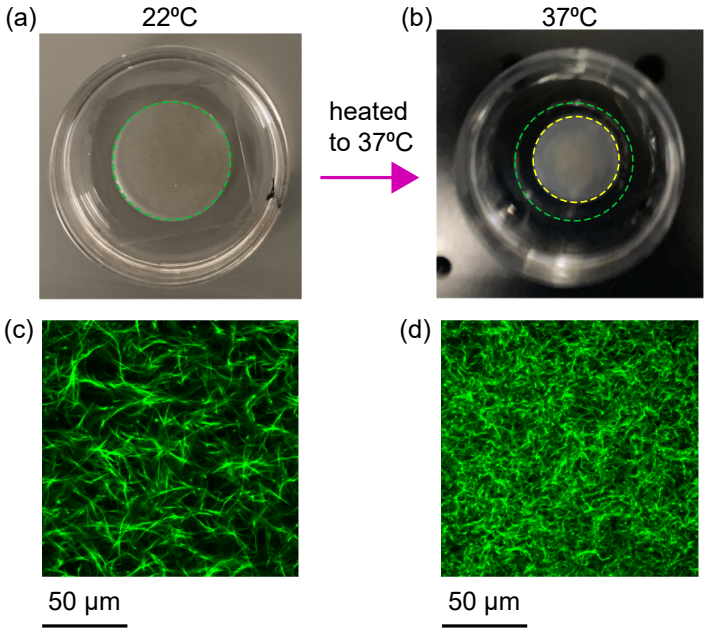

Figure S10. Representative collagen matrix with embedded PNIPAAm microspheres at different temperatures. (a) The disk-shaped collagen matrix with embedded PNIPAAm microspheres at room temperature (22°C), before contraction of the microspheres. The periphery of the matrix is highlighted by a green dashed circle. (b) When the temperature of the matrix was elevated to 37°C, the embedded PNIPAAm microspheres contracted triggering a global radial contraction of the matrix by 27%. The periphery of the contracted matrix is highlighted by a yellow dashed circle. (c) Representative confocal microscope image of matrix fibers at the top surface of the matrix shown in panel a. (d) Representative confocal microscope image of matrix fibers at the top surface of the contracted matrix of panel b. The spatial density of fibers is higher in panel d compared to panel c.

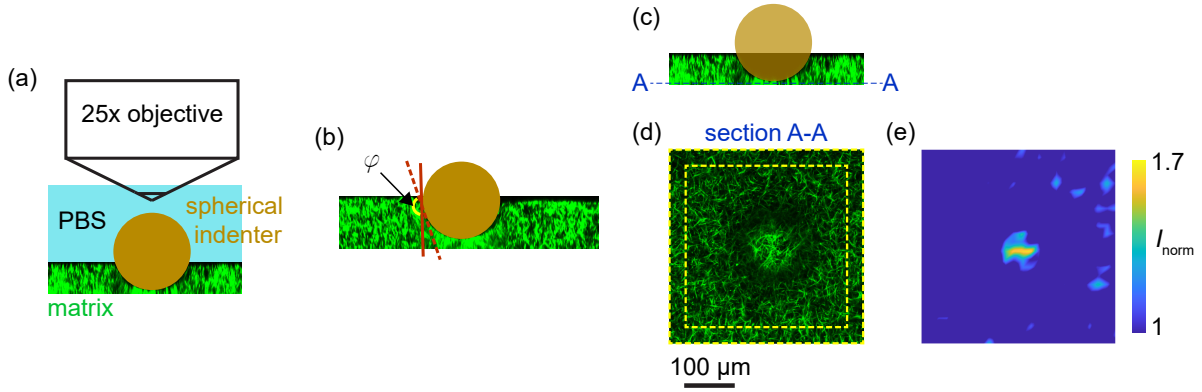

Figure S11. Some features of the microscopic indentation tests on collagen matrices. (a) The experimental setup of the sample matrix on the upright confocal microscope equipped with a 25× water immersion objective. Note that the surface of the collagen matrix had been indented with a spherical indenter and the matrix remained entirely submerged inside 1× PBS, while the lens of the objective was dipped inside the PBS above the indenter. (b) The obtuse contact angle ($\varphi > 90°$) between the surfaces of the collagen matrix and the spherical indenter depicting minimal adhesion between them. Contact angle φ is the angle between the tangents drawn on the surface of the indenter (solid line) and the matrix (dashed line) at their point of contact. (c) The *xz*-section of the surface of the matrix with the indenter. One *x*–*y* image plane passing through the matrix just below the indenter was identified (A–A). (d) The matrix image at plane A–A labeled in panel c. There exists a notable densification in the fibrous matrix just below the indenter. (e) The fluorescence intensities of the collagen fibers (of panel d) were spatially averaged over small subsets (32×32 pixels or 16×16 μm^2) across the image plane as an indicator of the local fiber density. The fiber density is maximum just below the indenter. The mapped average intensity values were normalized (I_{norm}) by the average intensity of the periphery of the matrix far away from the indenter; that peripheral region is highlighted by the dashed yellow boundaries near the edges of the image in panel d.

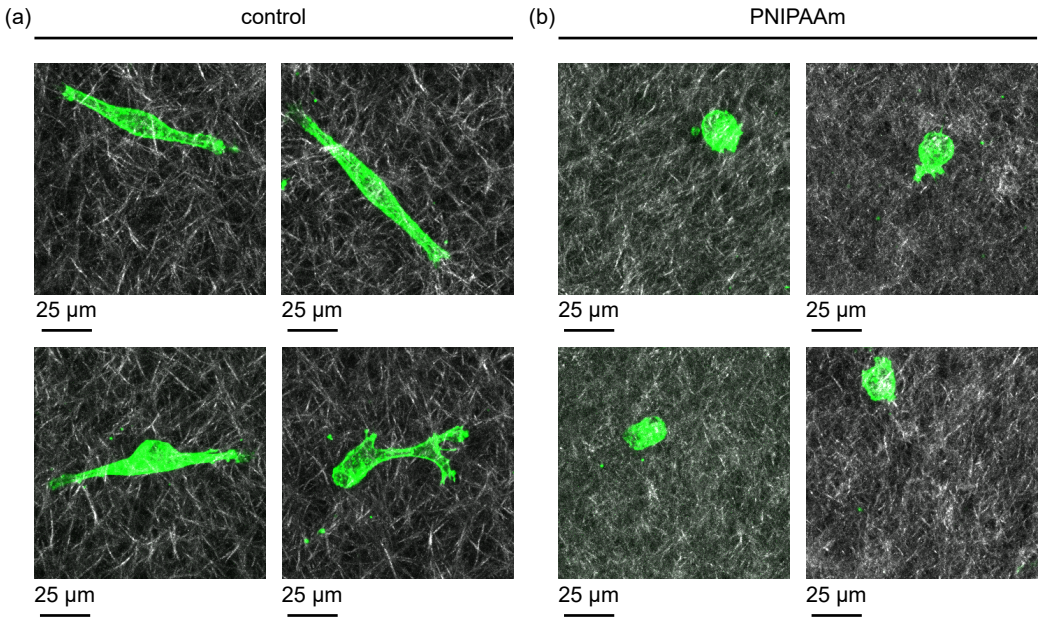

Figure S12. Additional representative images of MDA-MB-231 cells in the experiments depicting stiffness sensing by cells. (a) Elongated morphology of several independent cells in the control matrix of collagen,

with no embedded PNIPAAm microspheres at 37°C. (b) Rounded morphology of several independent cells in the PNIPAAm-embedded collagen matrix, when the embedded PNIPAAm microspheres contracted at 37°C, thereby causing matrix softening.

Supplemental Note 1: Comparison between Two and Three Dimensions

Two-dimensional (2D) fiber network models are numerically efficient and they can qualitatively match the nonlinear mechanics of three-dimensional (3D) biopolymer matrices made of collagen and fibrin. Prior studies [1, 2] documented that 2D models can capture many salient features of global nonlinearity of 3D matrices. Firstly, 2D models exhibit similar proportionality of the tangent modulus to the applied engineering stress as observed in 3D matrices. Secondly, the phenomenon of strain-induced matrix stiffening exhibited by 3D matrices is also well mimicked in 2D models. In addition to capturing global strain stiffening, 2D models are also able to simulate the evolution of the local microstructure of a deforming 3D matrix. For example, in a deforming matrix, fiber buckling has a large effect on the nonlinear mechanical response, and as prior studies have noted, 2D models can simulate effects of fiber buckling, such as long range propagation of displacements [3–5].

In this light, we used a 2D model in this study to make conceptually new predictions, followed by testing those predictions experimentally. The 2D simulations and 3D experiments do not give an exact quantitative match, however, which we describe further here. In the 2D simulations, the matrix globally contracted with engineering strains of $\approx 10\%$ in both the x and y directions (Fig. 2b). Under these conditions, there was substantial softening in the matrix, by a factor of nearly 5 on average (Fig. 2e). In the experiments with contracted PNIPAAm-embedded matrices, the matrices exhibited higher global radial contraction (radial strain of $\approx 27\%$, Supplemental Fig. S10b), but the extent of softening was a factor of ≈ 2 (Fig. 5m), indicating a lesser extent of softening as compared to the 2D simulations. The reduction in softening in 3D compared to 2D may be the result of less buckling in 3D matrices compared to 2D, which may come from the fact that displacements due to contracting inclusion decay faster over space in 3D elasticity as compared to 2D elasticity. Despite these differences between the 2D simulations and 3D experiments, the general trends, namely contracting inclusions causing softening due to fiber buckling, were consistent in two and three dimensions.

Supplemental Note 2: Comparison to Models Showing Fiber Alignment into Dense Bands

Prior studies have shown that, between pairs of contracting cells, dense bands of aligned fibers often form [3, 6–10]. These dense bands were not present in our model or experimental system, which may seem surprising, given the large number of prior studies observing them. An important difference between our modeling approach and that of prior studies is exactly how the contraction was simulated. Our model simulated the inclusions as an elastic body undergoing thermal contraction while enforcing both force equilibrium and kinematic compatibility in the system. By contrast, many prior studies implemented contraction of inclusions by moving the nodes on the boundary of each inclusion [3, 11–14], which enforces kinematic compatibility, but the inclusion itself is not necessarily in a state of equilibrium.

To demonstrate the effects of the different implementations, we used the system of two contracting inclusions and compared the two methods of imposing contraction, namely a thermal strain and a displacement boundary condition. External boundaries of the fiber network were left free. Results showed that under the thermal boundary condition, the separation distance between contracting inclusions (which we refer to as d_1 for the case of the thermal boundary condition) decreased, which was required to maintain force equilibrium within each contracting inclusion. By contrast, under the nodal displacement boundary condition, force

equilibrium of the contracting inclusions is not required, and the imposed boundary conditions artificially inhibit the distance between inclusions from decreasing. Consistent with this reasoning, when the nodal displacement boundary condition was used with the exact same fiber network, the separation distance (which we refer to as d_2 for the displacement boundary condition) did not decrease. This observation, $d_1 < d_2$, was consistent in multiple different fiber networks (Supplemental Fig. S5a–h). Additionally, for the case of the displacement boundary condition, the fibers were strongly densified and aligned between the contracting inclusions (Supplemental Fig. S5e–h). To quantify the changes in distance d_1 and d_2 and the fiber densification, we computed the normal strains in the region between the contracting inclusions in directions parallel to and transverse to the axis connecting the inclusions, ε_{xx} and ε_{yy}, respectively (Supplemental Fig. S5i). For the thermal boundary condition, the parallel strain ε_{xx} was near zero and sometimes negative, consistent with the inclusions moving closer together, whereas for the displacement boundary condition, ε_{xx} was notably larger. The transverse strain ε_{yy} was also notably different between the two cases, as it was strongly negative for the displacement boundary condition and less negative for the thermal boundary condition. The strongly negative strain for the displacement boundary condition is consistent with a substantial increase in local density, which quantitatively confirms that dense bands of aligned fibers formed between contracting inclusions in the displacement boundary condition case.

In summary, our model is able to capture the formation of dense fiber bands observed in prior models when using the displacement boundary condition, as done by the prior models. However, we do not expect substantial band formation to occur in a real material at these strains in a system with unconstrained external boundaries, because the more accurate thermal boundary condition predicts no band formation at this level of strain. For bands to form, a greater magnitude of contractile strain would be necessary.

Supplemental Note 3: Cell Morphology is Likely Invariant to the Collagen Density

While the results described in Fig. 6a–d would seem to suggest that the cell morphology is affected by the softening of the matrix due to the contractile PNIPAAm microspheres, it is important to also consider another factor, which is that the contracted matrices also had a higher spatial density of fibers (Supplemental Fig. S10). The relationship between cellular morphology and fiber density is complicated, as it is biphasic, with the greatest cellular elongation occurring at a collagen concentration of ≈ 1 mg/mL, and elongation diminishing with collagen concentration for concentrations in the range of 1–2 mg/mL, and elongation almost invariant to collagen concentration for concentrations above 2 mg/mL [15–17]. As the collagen matrices we prepared had a concentration of 3 mg/mL and the contraction caused by the PNIPAAm microspheres further increased the concentration, our experiments were in the regime wherein collagen concentration would not be expected to affect cell morphology, indicating that the different fiber concentrations in this experiment were unlikely to have altered the cellular morphology. Therefore, the changes in cellular morphology in our contracted matrices were most likely tuned by the decrease in the stiffness of the matrix.

References

[1] A. J. Licup, S. Münster, A. Sharma, M. Sheinman, L. M. Jawerth, B. Fabry, D. A. Weitz, F. C. MacKintosh, Stress controls the mechanics of collagen networks, P Natl Acad Sci USA 112 (31) (2015) 9573–9578.

[2] M. Sarkar, J. Notbohm, Evolution of force chains explains the onset of strain stiffening in fiber networks, J Appl Mech 89 (11) (2022) 111008.

[3] J. Notbohm, A. Lesman, P. Rosakis, D. A. Tirrell, G. Ravichandran, Microbuckling of fibrin provides a mechanism for cell mechanosensing, J R Soc Interface 12 (108) (2015) 20150320.

[4] P. Grimmer, J. Notbohm, Displacement propagation in fibrous networks due to local contraction, J Biomech Eng—T ASME 140 (4) (2018) 041011.

[5] S. Goren, Y. Koren, X. Xu, A. Lesman, Elastic anisotropy governs the range of cell-induced displacements, Biophys J 118 (5) (2020) 1152–1164.

[6] D. Stopak, A. K. Harris, Connective tissue morphogenesis by fibroblast traction: I. Tissue culture observations, Dev Biol 90 (2) (1982) 383–398.

[7] T. Korff, H. G. Augustin, Tensional forces in fibrillar extracellular matrices control directional capillary sprouting, J Cell Sci 112 (19) (1999) 3249–3258.

[8] D. Vader, A. Kabla, D. Weitz, L. Mahadevan, Strain-induced alignment in collagen gels, Plos One 4 (6) (2009) e5902.

[9] Q. Shi, R. P. Ghosh, H. Engelke, C. H. Rycroft, L. Cassereau, J. A. Sethian, V. M. Weaver, J. T. Liphardt, Rapid disorganization of mechanically interacting systems of mammary acini, P Natl Acad Sci USA 111 (2) (2014) 658–663.

[10] S. Natan, Y. Koren, O. Shelah, S. Goren, A. Lesman, Long-range mechanical coupling of cells in 3d fibrin gels, Mol Biol Cell 31 (14) (2020) 1474–1485.

[11] D. Humphries, J. Grogan, E. Gaffney, Mechanical cell–cell communication in fibrous networks: the importance of network geometry, Bull Math Biol 79 (2017) 498–524.

[12] R. S. Sopher, H. Tokash, S. Natan, M. Sharabi, O. Shelah, O. Tchaicheeyan, A. Lesman, Nonlinear elasticity of the ecm fibers facilitates efficient intercellular communication, Biophys J 115 (7) (2018) 1357–1370.

[13] E. Ban, J. M. Franklin, S. Nam, L. R. Smith, H. Wang, R. G. Wells, O. Chaudhuri, J. T. Liphardt, V. B. Shenoy, Mechanisms of plastic deformation in collagen networks induced by cellular forces, Biophys J 114 (2) (2018) 450–461.

[14] E. Ban, H. Wang, J. M. Franklin, J. T. Liphardt, P. A. Janmey, V. B. Shenoy, Strong triaxial coupling and anomalous poisson effect in collagen networks, P Natl Acad Sci USA 116 (14) (2019) 6790–6799.

[15] Y. Wu, M. R. Zanotelli, J. Zhang, C. A. Reinhart-King, Matrix-driven changes in metabolism support cytoskeletal activity to promote cell migration, Biophys J 120 (9) (2021) 1705–1717.

[16] M. Baday, O. Ercal, A. Z. Sahan, A. Sahan, B. Ercal, H. Inan, U. Demirci, Density based characterization of mechanical cues on cancer cells using magnetic levitation, Adv Healthc Mater 8 (10) (2019) 1801517.

[17] D. L. Matera, W. Y. Wang, M. R. Smith, A. Shikanov, B. M. Baker, Fiber density modulates cell spreading in 3D interstitial matrix mimetics, ACS Biomater Sci Eng 5 (6) (2019) 2965–2975.